

**EXPERIMENTAL IMPLEMENTATION OF
HIGHER DIMENSIONAL ENTANGLEMENT**

NG TIEN TJUEN

(B.Sc. (Hons.)), NUS

**A THESIS SUBMITTED FOR THE DEGREE OF
MASTER OF SCIENCE**

**PHYSICS DEPARTMENT
NATIONAL UNIVERSITY OF SINGAPORE**

2013

Declaration

I hereby declare that this thesis is my original work and it has been written by me in its entirety. I have duly acknowledged all the sources of information which have been used in the thesis.

This thesis has also not been submitted for any degree in any university previously.



Ng Tien Tjun
1 October 2013

Acknowledgements

Firstly, I would like to extend my heartfelt thanks and gratitude to my senior Poh Hou Shun, whom I have the pleasure of working with on various experiments over the years. They have endured with me through endless days in the laboratory, going down numerous dead ends before finally getting the experiments up and running. Special thanks also to my project advisor, Christian Kurtsiefer for his constant guidance over the years. Thanks also goes out to Cai Yu from the theory group for proposing this experiment and Chen Ming for giving me valuable feedback on the experimental and theoretical skills.

A big and resounding thanks also goes out to my other fellow researchers and colleagues in quantum optics group. Thanks to Syed, Brenda, Gleb, Peng Kian, Siddarth, Bharat, Gurpreet, Victor and Kadir. They are a source of great inspiration, support, and joy during my time in the group.

Finally, I would like to thank my friends and family for their kind and constant words of encouragement.

Contents

1	From Quantum Theory to Physical Measurements	1
1.1	Aim of this Thesis	3
2	Theoretical Background	5
2.1	Entanglement	5
2.2	Bell Inequalities	7
2.2.1	CGLMP Inequality	9
2.2.2	Derivation of the 4-Dimensional CGLMP Inequality .	14
3	Generation of Entangled Photon Pairs	19
3.1	Entangled Photon Pairs	19
3.1.1	Second-Order Non-linear Optical Phenomena	20
3.2	Generation of Polarization-Entangled Photon Pairs	21
3.2.1	Longitudinal and Transverse Walk-Off	23
3.2.1.1	Compensation of Longitudinal (Temporal) Walk-Off	23
3.2.1.2	Compensation of Transverse (Spatial) Walk- Off	24
3.2.2	Characterization of Polarization-Entangled Photon Pairs	26
3.3	Generation of Energy-time Entanglement	27
3.3.1	Time-bin Entanglement	29
3.3.2	Characterization of Energy-time Entangled Photon Pairs	31
3.4	Entanglement in a High-Dimensional Bipartite System	32

CONTENTS

4	Implementation of Sources of 2-Dimensional Entangled Photon States	35
4.1	Photon Pairs Collection	36
4.2	Characterization of Detector Efficiency	39
4.3	Polarization-Entangled Photons	42
4.3.1	Polarization Correlation	44
4.4	Energy-time Entangled Photons	46
4.4.1	Consideration of Interferometer Type	46
4.4.2	Schematic of Setup for Generation Energy-Time Entangled Photons	48
4.4.3	Matching the Interferometer Path Length Differences	49
4.4.4	Coincidence Time Window	55
4.4.5	Energy-time Correlation	58
4.5	Summary	61
5	Violation of the 4-Dimensional CGLMP Inequality	63
5.1	Background	63
5.2	Implementation of 4-Dimensional Entangled Photons	64
5.2.1	Optimizing the Quality of the Interferometers	66
5.2.2	Phase Shift Compensation	67
5.2.3	Quality of the 4-dimensional Entangled State	70
5.2.4	Piezoelectric Actuator	70
5.2.5	Stabilizing the Interferometers	72
5.3	Measurement Settings	74
5.4	Experimental Results & Conclusions	77
6	Final Remarks	79
	Bibliography	81

Summary

This thesis documents my research on setting up a source of polarization and energy-time entangled photons. The photon pairs are produced by a spontaneous parametric down-conversion (SPDC) process. I will focus on the preparation and characterization of these sources. The goal of this research is to produce high-dimensional entanglement which can be used for various quantum communication protocols and fundamental tests of quantum physics. The combination of polarization and energy-time degrees of freedom allows us to prepare hyperentanglement with a dimensionality of 4. The choices of the degrees of freedom of the experimental setup are discussed in detail.

The non-classical correlations from entangled photon pairs are useful for studying the dimensionality of a system without assumptions as in most theoretical models. For certain systems it is possible to determine the presence of entanglement in higher dimensions by appealing to a dimension witness like the CGLMP inequality. In the last part of the thesis, I will present results from a dimension witness experiment carried out and conclude with some remarks on the remaining issue known to be restricting the quality of the source.

CONTENTS

Chapter 1

From Quantum Theory to Physical Measurements

The development of quantum mechanics driven by Bohr, Heisenberg, Pauli, Schrödinger *et al.* in the beginning of the 20th century has suggested a strange and weird picture which is not directly accessible in daily life. The probabilistic description of the properties of physical objects (momentum, position,...) is in contradiction with the deterministic nature of classical physics, whereby these properties have well-defined values. Quantum theory contains observables which correspond to measurable physical quantities. Heisenberg's uncertainty principle states that there are specific pairs of physical observables which cannot be determined with absolute certainty [1]. There is no analogue of this principle in classical physics.

Quantum theory predicts the phenomenon whereby two particles remain perfectly correlated over arbitrarily large distances. This is called entanglement and was described as a “spooky action at a distance” by Einstein. A physical system consisting of two or more entities cannot be described by only considering each of the component entity alone. Instead, a full description of this physical system is only possible by considering the system as a whole. Entanglement has proven to be suitable for performing tasks which were impossible according to classical mechanics. Unlike the classical bit which only allows one value; either state 0 or 1 to be stored, the quantum bit or qubit can be prepared in a superposition state:

1. FROM QUANTUM THEORY TO PHYSICAL MEASUREMENTS

$\alpha|0\rangle + \beta|1\rangle$, where $|\alpha|^2 + |\beta|^2 = 1$. The probability amplitudes α and β are generally complex numbers. A two level quantum system is an implementation of qubits, which is an essential building block for quantum information [2]. Entanglement provides the fundamental key component for the development of quantum information, a fusion between the fields of quantum physics, information theory, computation, and communication.

The experimental realization of quantum information sciences in recent years was demonstrated with several quantum protocols. The development of quantum algorithms such as the Shor algorithm [3, 4] and Grover search [5, 6] improve the efficiency of information processing. Quantum information sciences also secure transmission of classical information (quantum cryptography) [7, 8], transfer of quantum states between distant locations (quantum teleportation) [9, 10] and an increase in communication channel capacity (dense coding) [11, 12]. These applications provided a boost to research in experimental quantum systems. Various degrees of freedom available in quantum systems are used to encode qubits. Some of these first experiments used the polarization [13, 14, 15, 16], energy-time [17, 18, 19], time-bin [20, 21], and orbital angular momentum [22, 23] of photons to encode the photonic qubit. The photonic qubits are easily and accurately manipulated using linear and non-linear optical devices because these techniques require classical optics which have been studied in detail.

The amount of information being transmitted and processed is a fundamental resource in quantum communication and computation. A high-dimensional entangled state can transmit more information than conventional two-dimensional systems. This reduces the noise threshold limiting the security of quantum key distribution (QKD) protocols [24, 25, 26, 27]. Furthermore, high-dimensional entangled states also lower the threshold of the detection efficiency for loophole free Bell experiments [28] which demonstrate the phenomenon of entanglement in quantum mechanics and it shows that the results cannot be explained by local realistic theories. The dimensionality of a system, *i.e.* the number of independent degrees of freedom needed to completely describe it, is one of the most basic concepts in science. Most theoretical models place assumptions on the dimensionality of a system. It would be desirable to assess the dimensionality of a

system without assumptions. The challenge is to assess the dimension of a set of states without referring to the internal working of the device. One such class of measurements are the dimension witnesses. They provide a lower bound on the dimensionality of a system by appealing to statistics from specific measurements [29]. The analysis of higher-dimensional entanglement becomes complex, both theoretically and experimentally. It is not easy to distinguish between classical and quantum correlations in a higher-dimensional systems. Moreover, the number of operations needed to determine properties of the state increases with the number of dimensions. In practice, a large number of resources are needed to investigate high-dimensional entanglement. Hence, it is both interesting and relevant to investigate how much one can learn about high-dimensional entanglement from a limited set of measurements. The study and experimental realization of higher dimensional entanglement will be the main focus of this work.

1.1 Aim of this Thesis

In this thesis, we aim to experimentally prepare a 4-dimensional hyper-entangled state (ququad) by entangling the polarization and energy-time degrees of freedom of photons generated from spontaneous parametric down-conversion (SPDC). The generated ququad is then used to test the 4-dimensional CGLMP inequality [30]. Violation of this inequality will allow us to set the lower bound of the dimension of the Hilbert space describing the system.

In Chapter 2, we first review the theoretical framework of the CGLMP inequality and describe its possible application as a dimensional witness. We then continue in Chapter 3 with a detailed overview on the process of SPDC. This is followed by an experimental study of the polarization and energy-time entangled source of photon pairs in Chapter 4. Lastly in Chapter 5, we will present an experiment violating the 4-dimensional CGLMP inequality before ending with some final remarks about the remaining issues limiting this experiment in Chapter 6.

1. FROM QUANTUM THEORY TO PHYSICAL MEASUREMENTS

Chapter 2

Theoretical Background

In this chapter we will cover the basic theory behind entanglement followed by a brief description of Bell's inequalities. This is followed by an indepth overview of the CGLMP inequality. Finally, we will present a detailed derivation of the maximum violation of the CGLMP inequality for a 4-dimensional (ququad) maximally entangled state. In so doing, we will also demonstrate the viability of using the CGLMP inequality as a dimensional witness for the 4-dimensional entangled state.

2.1 Entanglement

A state $|\psi\rangle$ in the Hilbert space $H = H_A \otimes H_B$ is called separable when: $|\psi\rangle_A \in H_A$ and $|\psi\rangle_B \in H_B$ such that $|\psi\rangle = |\psi\rangle_A \otimes |\psi\rangle_B$. Otherwise the state is called entangled. Only quantum mechanics allows the existence of entangled states because they exhibit correlations that have no classical analogue. The finite-dimensional bipartite quantum system is a system composed of two distinct subsystems, i.e. $|\psi\rangle = \alpha|i\rangle_A|i\rangle_B + \beta|j\rangle_A|j\rangle_B$, whereby the states $\{|i\rangle_A, |j\rangle_A\} \in H_A$ and $\{|i\rangle_B, |j\rangle_B\} \in H_B$ with $(i, j) = \{0, 1\}$, with a dimensionality of $N = 2$ in the Hilbert space. A measurement on the system H_A instantly determines the measurement outcome on the system H_B with absolute certainty. Quantum systems consisting of two or more entities can no longer be described by considering each of the component entities in isolation. A full description of such a composite

2. THEORETICAL BACKGROUND

quantum system is only possible by considering the system as a whole.

The term “entanglement”, used in quantum mechanics to describe this inseparable relationship between quantum systems, was introduced by Schrödinger in 1935. He believed that entanglement was one of the most important aspects of the quantum world, describing it as “the characteristic trait of quantum mechanics, the one that enforces its entire departure from classical lines of thought.” [31]. The introduction of entanglement was shortly after Einstein, Podolsky, and Rosen (EPR) formulated a thought experiment that attempted to show that quantum theory is incomplete [32]. At the time when the EPR paper was written, the Heisenberg’s uncertainty principle [1], which states that complementary properties of a particle such as its position and momentum cannot be ascertained simultaneously with absolute precision, was already known. However, Einstein believed there exists an underlying physical reality, in which all the physical objects must have well defined position and momentum and evolve according to deterministic classical laws.

The EPR paper considered the case of a pair of spatially well separated (no longer interacting) particles A and B, which have previously interacted. Due to the conservation of momentum, these particles have perfectly correlated momenta and positions. Thus the wavefunction of the pair of particle cannot be written as a product of the wavefunctions of the individual particles.

If the momentum of particle A is measured, the momentum of particle B is determined with certainty due to the momentum correlation. Similarly, if the position of particle B is measured, the position of particle A is determined with certainty due to the position correlation. Thus both the complementary properties of the two particles are known with absolute precision. This is in contradiction with the uncertainty principle, a fundamental principle of quantum theory. EPR tried to set up a paradox to conclude that the quantum mechanical description of physical reality given by wave functions is not complete and thus suggests that quantum theory is incomplete as well.

In order to fully account for the joint properties of the particles under the framework of classical physics, the EPR paper proposed that additional parameters must be supplemented into the description of physical objects.

The possible explanation is that the information about the outcome of all possible measurements was already present in both systems. Since the outcome of a measurement was claimed to be known before the measurement takes place, there must exist something in the real world, hidden variables, which predetermine the measurement outcomes.

2.2 Bell Inequalities

In 1964, John S. Bell proposed the Bell inequality [33, 34] which allows the predictions of quantum mechanics and hidden variable theories to be distinguished. In brief, the original thought experiment proposed by Bell is that of a spin-1/2 system interacting at their joint emission point and propagating in opposite directions. The idea is based on arguments about measurement probabilities that result from classical correlations alone and imposes an upper limit for it. Quantum mechanics predicts stronger correlations and thus will violate this classical limit, demonstrating that prediction from quantum mechanics is in general incompatible with local hidden variable theory.

The most widespread version of Bell's inequality used in experimental tests is the one from Clauser, Horne, Shimony and Holt known as the CHSH inequality which requires only two measurement settings per observer [35]. This can be implemented experimentally by measuring the polarization correlations of an entangled pair of photons. The CHSH inequality, as with Bell's original inequality includes experimentally determinable quantities to be measured. The spin-1/2 system is a bipartite system, with two measurement settings and two possible outcomes on each side. The correlation function is determined experimentally by averaging the outcomes of two local observables giving the probability of obtaining a particular outcome. The CHSH inequality includes a parameter S which is defined by

$$S = E(\theta_1, \theta_2) - E(\theta_1, \theta'_2) + E(\theta'_1, \theta_2) + E(\theta'_1, \theta'_2), \quad (2.1)$$

where $E(\theta_1, \theta_2)$ is the correlation function for measurements with only two

2. THEORETICAL BACKGROUND

possible outcomes. This is given by

$$E(\theta_1, \theta_2) = P(\uparrow\uparrow | \theta_1, \theta_2) + P(\downarrow\downarrow | \theta_1, \theta_2) - P(\uparrow\downarrow | \theta_1, \theta_2) - P(\downarrow\uparrow | \theta_1, \theta_2), \quad (2.2)$$

where $P(\uparrow\uparrow | \theta_1, \theta_2)$ is the probability of obtaining spin-up for both particles with measurement settings θ_1 and θ_2 respectively (Fig. 2.1). A value of $|S| \leq 2$ does not allow us to distinguish the prediction of quantum correlation from that of classical correlation. A quantum correlation will result in the violation of this inequality. On the other hand a theoretical absolute maximum violation of the CHSH inequality with a value of $|S| = 2\sqrt{2}$ can be obtained with a maximally entangled 2-dimensional state. It can also be shown that this maximum violation of CHSH inequality decreases with the increase in the dimensionality of the entangled state. This feature renders the CHSH inequality ineffective as a test for the dimensionality of an entangled state; it is impossible to distinguish between a violation due to a higher dimensional entangled state and lower dimensional non-maximally entangled state.

In 1982, a direct test of CHSH Bell type inequalities was carried out by Alain Aspect *et al.* [36] whereby the result obtained supported the predictions of quantum mechanics. It is worth noting that all current experimental tests of Bell's inequalities take place with imperfect experimental devices which allow for loophole arguments. The experiments often have low detection efficiency (detection loophole) and the two measurement parties are not placed sufficiently far apart (locality loophole). These loopholes have been covered in separate experiments [37, 38] but no experiment to date has been performed to simultaneously address these two loopholes. The extent to which quantum states can violate a given Bell inequality was investigated soon after that since it is impossible in practice to prepare pure entangled states with no noise. The strength of the violation decreases if there is a mixture of noise which reduces quantum correlations. Therefore, a stronger violation corresponds to the most robust quantum correlations against a mixture of noise. In 2000, the investigation of the violation of local realism by two entangled N -dimensional systems by Kaszlikowski *et al.* [39] was proved to be stronger for increasing values of N . Hence, quantum correlations get more robust against a mixture of noise as

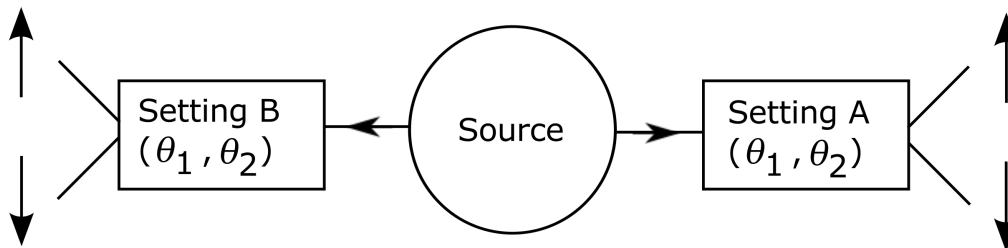


Figure 2.1: A spin-1/2 system with two measurement settings θ_1, θ_2 and two outcomes \uparrow, \downarrow on each side. The four different combinations of settings give a total of 16 coincidence measurements which are used for calculating the Bell inequality.

the dimension of the system N increases.

2.2.1 CGLMP Inequality

In 2002, a set of Bell's inequalities known as the CGLMP inequality was proposed by Daniel Collins, Nicolas Gisin, Noah Linden, Serge Massar, and Sandu Popescu [30]. Within the framework of quantum mechanics, a strong violation of such an inequality indicates that the state is not only entangled, but also that the entanglement is of a particular dimensional system. These inequalities are generalised for arbitrary high-dimensional bipartite systems with two measurement settings and d outcomes on each side. In a bipartite system, suppose that one of the parties, Alice, can carry out two possible measurements, A_1 or A_2 , and that the other party, Bob, can also carry out two possible measurements, B_1 or B_2 . Each measurement may have d possible outcomes: $A_1, A_2, B_1, B_2 = 0, \dots, d-1$, see Fig. 2.2. The CGLMP expression has the form,

$$\begin{aligned}
 I_d \equiv \sum_{k=0}^{\lfloor d/2 \rfloor - 1} \left(1 - \frac{2k}{d-1} \right) \{ & [P(A_1 = B_1 + k) + P(B_1 = A_2 + k + 1) \\
 & + P(A_2 = B_2 + k) + P(B_2 = A_1 + k)] \\
 & - [P(A_1 = B_1 - k - 1) + P(B_1 = A_2 - k) \\
 & + P(A_2 = B_2 - k - 1) + P(B_2 = A_1 - k - 1)] \},
 \end{aligned} \tag{2.3}$$

2. THEORETICAL BACKGROUND

where $P(A_a = B_b + k)$ is the probability that the measurements A_a and B_b have outcomes that differ by k modulo d ,

$$P(A_a = B_b + k) \equiv \sum_{j=0}^{d-1} P(A_a = j, B_b = j + k \bmod d). \quad (2.4)$$

with $d \geq 2$. For any values of d , the measurements with $I_d(\text{LHV}) \leq 2$ is an upper bound on the correlations between measurement results under the assumption of local hidden variable (LHV) theory. For two outcomes

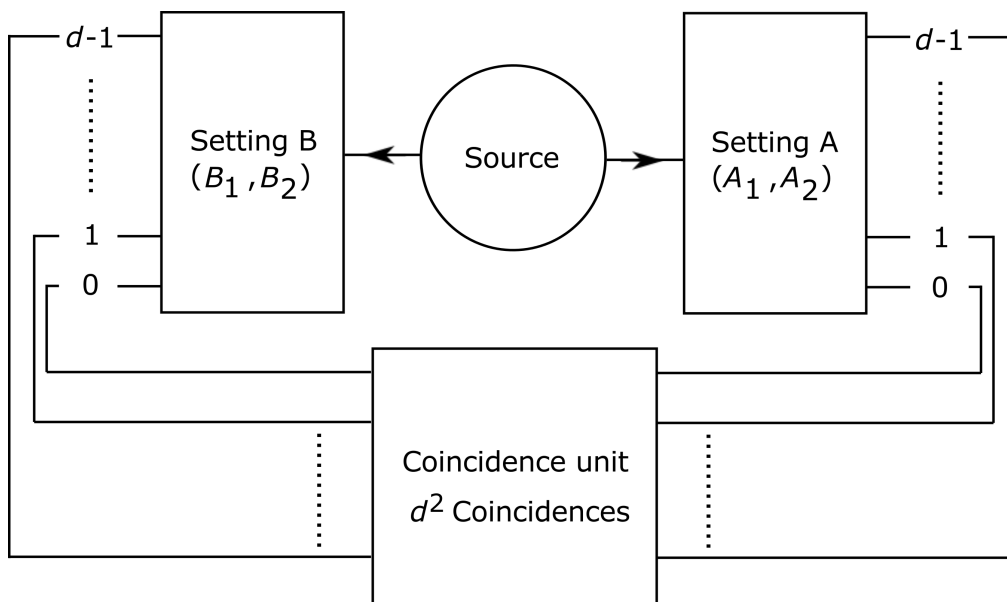


Figure 2.2: A d dimensional quantum system with two measurement settings and d outcomes on each side. The four different combinations of settings give in total of $4d^2$ coincidences which are used for calculating the CGLMP inequality.

$d = 2$, the Bell expression is written as,

$$\begin{aligned} I_2 = & [P(A_1 = B_1) + P(B_1 = A_2 + 1) + P(A_2 = B_2) + P(B_2 = A_1)] \\ & - [P(A_1 = B_1 - 1) + P(B_1 = A_2) + P(A_2 = B_2 - 1) \\ & + P(B_2 = A_1 - 1)] \end{aligned}$$

$$\begin{aligned}
&= P(A_1 = 0, B_1 = 0) + P(A_1 = 1, B_1 = 1) + P(A_2 = 0, B_1 = 1) \\
&\quad + P(A_2 = 1, B_1 = 0) + P(A_2 = 0, B_2 = 0) + P(A_2 = 1, B_2 = 1) \\
&\quad + P(A_1 = 0, B_2 = 0) + P(A_1 = 1, B_2 = 1) - P(A_1 = 0, B_1 = 1) \\
&\quad - P(A_1 = 1, B_1 = 0) - P(A_2 = 0, B_1 = 0) - P(A_2 = 1, B_1 = 1) \\
&\quad - P(A_2 = 0, B_2 = 1) - P(A_2 = 1, B_2 = 0) - P(A_1 = 0, B_2 = 1) \\
&\quad - P(A_1 = 1, B_2 = 0) \\
&= E(A_1, B_1) + E(A_2, B_2) + E(A_1, B_2) - E(A_2, B_1) \\
&= S,
\end{aligned}$$

which is equivalent to the CHSH expression (Eq. 2.1).

Indeed, as the dimension of the Hilbert space increases, the maximal violation found for a maximally-entangled state

$$|\Phi_d^+\rangle = \frac{1}{\sqrt{d}} \sum_{j=0}^{d-1} |j\rangle_A \otimes |j\rangle_B, \quad (2.5)$$

increases. It is important to note for a given d , $|\Phi_d^+\rangle$ does not give the maximum violation [40, 41, 42]. A larger violation or equivalently a stronger resistance to noise, is found for non-maximally entangled states except when $d = 2$ [40]. In this thesis, we focus on the 4-dimensional bipartite system with two measurement settings on both parties. Alice performs two possible measurements, A_1 or A_2 , and Bob performs two possible measurements, B_1 or B_2 . Each measurement has 4 possible outcomes or $d = 4$. For $d = 4$, the CGLMP expression thus contains 64 probabilities as one might expect and the measurement of the CGLMP inequality becomes increasingly hard as the dimension of the output increases.

The computation of this high-dimensional Bell's inequalities has been the subject of several studies in recent years. Numerical studies [43, 44] have provided an unexpectedly simple expression for this CGLMP expression. Let $P_{AB}^{o_a o_b}(s_a, s_b)$ be the joint probability of Alice's outcome o_a with the measurement setting s_a and Bob's outcome o_b with the measurement setting s_b , where $o = 1, \dots, d$ and $s = 1, 2$ for two measurement settings. Suppose Alice and Bob have m_A and m_B possible measurement settings that would each generate d_A and d_B outcomes, respectively. Denote $\mathbf{m} \equiv (m_A, m_B)$ and $\mathbf{d} \equiv (d_A, d_B)$, a compact description of the number of

2. THEORETICAL BACKGROUND

local measurement settings and the number of possible outcomes for each local measurement. A simplified and equivalent CGLMP expression $I_{m;d}$ with two measurement settings $m_A = m_B = 2$ and d possible outcomes, $d_A = d_B = d$ is defined as [45],

$$\begin{aligned}
 I_{22dd}(\text{LHV}) = & \sum_{o_a=1}^{d-1} \sum_{o_b=1}^{d-o_a} P_{AB}^{o_a o_b}(1, 1) + \sum_{o_a=1}^{d-1} \sum_{o_b=d-o_a}^{d-1} [P_{AB}^{o_a o_b}(1, 2) + P_{AB}^{o_a o_b}(2, 1) \\
 & - P_{AB}^{o_a o_b}(2, 2)] - \sum_{o_a=1}^{d-1} P_A^{o_a}(1) - \sum_{o_b=1}^{d-1} P_B^{o_b}(1) \leq 0. \quad (2.6)
 \end{aligned}$$

For two outcomes $d = 2$, the above expression is written as,

$$\begin{aligned}
 I_{2222}(\text{LHV}) = & P_{AB}^{11}(1, 1) + P_{AB}^{11}(1, 2) + P_{AB}^{11}(2, 1) + P_{AB}^{11}(2, 2) \\
 & - P_A^1(1) - P_B^1(1) \leq 0, \quad (2.7)
 \end{aligned}$$

which is known as the CH74 [46] inequality developed by Clauser and Horne in 1974. The distinction of this inequality is that it involves the measurement of non-joint probabilities. The CHSH inequality can be derived from the CH74 by adding the fair sampling assumption. The CH74 inequality is immune to fair sampling of the events and detection efficiency of the experiment. The I_{2222} contains only the measurement with one outcome $P_A^1(1)$ or $P_B^1(1)$, so whether or not the total measurement outcomes 1 and 2 represents a fair sample of the total events emitted from the source is irrelevant. Fair sampling takes into account no detection and double detection events in Alice and Bob's outcomes. It is considerably more general compared to the CHSH inequality but is difficult to implement in practice. This is because one would need ideal detectors to measure the total events received by Alice (Bob) in order to establish the quantity $P_A^1(1)$ ($P_B^1(1)$), however such events may not necessary show any outcome event on Bob's (Alice's) measurement.

The CGLMP expression Eq. 2.3 is equivalent to the I_{22dd} expression Eq. 2.7. The details of the proof can be found in [45]. These two inequalities are related as follows,

$$I_{22dd} = \frac{d-1}{2d}(I_d - 2). \quad (2.8)$$

$I_{22dd} \geq 0$ implies that local hidden variables are incompatible with quantum

2.2 Bell Inequalities

predictions. In the presence of white noise, the quantum state becomes

$$\rho(p) = p|\Phi_d^+\rangle\langle\Phi_d^+| + (1-p)\frac{\mathbb{I}_d \otimes \mathbb{I}_d}{d^2}, \quad (2.9)$$

where \mathbb{I} is the d dimensional identity matrix and p is the weight of the d dimensional maximally entangled state in the mixture. The CGLMP expression is certainly violated if $p > \frac{2}{I_d(\text{QM})} = p_w$.

Table 2.1 shows the summary of different types of violation with two measurement settings and d outcomes. It has been shown that the maximum CGLMP violation $I_d^{\max}(\text{QM})$ does not correspond to maximally entangled input states [40, 47]. $I_d^{|\Phi_d^+\rangle}$ is the maximum violation for an input state $|\Phi_d^+\rangle$ which is maximally entangled. $I_{22dd}^{|\Phi_d^+\rangle}$ is the corresponding best known I_{22dd} violation given in Eq. 2.8. Below the threshold weight p_w , no violation is expected. For $d \geq 2$, $I_d^{\max}(\text{QM})$ increases suggesting a larger

Table 2.1: CGLMP $I_d(\text{QM})$ and I_{22dd} violation [45].

d	$I_d^{\max}(\text{QM})$	$I_d^{ \Phi_d^+\rangle}$	$I_{22dd}^{ \Phi_d^+\rangle}$	p_w
2	2.8284	2.8284	0.20711	0.70711
3	2.9149	2.8729	0.29098	0.69615
4	2.9727	2.8962	0.33609	0.69055
5	3.0157	2.9105	0.36422	0.68716
6	3.0497	2.9202	0.38342	0.68488
7	3.0776	2.9272	0.39736	0.68326
8	3.1013	2.9324	0.40793	0.68203
9	3.1217	2.9365	0.41622	0.68108
10	-	2.9398	0.42291	0.68032
100	-	2.9668	0.47856	0.67413
1000	-	2.9695	0.48427	0.67351
∞	-	2.9698	0.48491	0.67349

violation could be possible by increasing the dimension of the system. The p_w values indicate that the CGLMP violation of higher dimensional systems are more resistant to noise.

2. THEORETICAL BACKGROUND

The violation of Bell-type inequalities indicate that a local hidden variable model cannot fully describe the situation and this can be seen as a non-classical property of quantum correlations. The violation also depends on the details of the particular Bell-type inequality that is tested. The CGLMP inequalities are generalised for arbitrary high-dimensional bipartite systems only. A high violation of CGLMP inequalities indicates that the state is entangled and the entanglement is of a particular dimensionality. The numerical proof shows the CGLMP violation is higher for an entangled state in a higher dimension even though the state is not maximally entangled.

In this thesis, we use the CGLMP inequality as a dimension witness for our ququad experiment. The idea of dimension witness is that there exists an upper bound of CGLMP violation if we restrict ourself to lower dimensional systems. In this particular case, the maximum violation of I_{2244} with qutrits, is strictly lesser than ququads. The maximal violation of I_{2244} with qutrits could be shown to identical to $I_{2233}^{max} = 0.304951$ [48, 49]. To summarize, for two measurement settings and four outcomes on each side, if the bound $I_{2233}^{max} \leq 0.304951$ is violated, the dimension of the entangled system under investigation is at least 4.

2.2.2 Derivation of the 4-Dimensional CGLMP Inequality

In this section, we describe the detailed steps to obtain $I_{2244} = 0.33609$ (in Table 2.1) for a 4-dimensional maximally-entangled state by using the CGLMP expression in Eq. 2.6. This I_{2244} will be useful later for comparison with our experimental results to verify if we indeed have a 4-dimensional maximally-entangled state. For the purpose of our derivation here, we start off by writing a 4-dimensional maximally entangled state,

$$|\Phi\rangle = \frac{1}{2} (|00\rangle + |11\rangle + |22\rangle + |33\rangle), \quad (2.10)$$

with the definitions:

$$\begin{aligned}|0\rangle &= (1, 0, 0, 0)^T \\ |1\rangle &= (0, 1, 0, 0)^T \\ |2\rangle &= (0, 0, 1, 0)^T \\ |3\rangle &= (0, 0, 0, 1)^T\end{aligned}$$

The detection probability (coincidence) between outcome $|k\rangle_{A,a}$ and $|l\rangle_{B,b}$ is written as

$$P_{AB}^{kl}(a, b) = \text{Tr}(|k\rangle_{A,a}\langle l|_{B,b} \langle k|_{A,a} \langle l|_{B,b} \rho). \quad (2.11)$$

2. THEORETICAL BACKGROUND

The corresponding density matrix is written as (for ease of reading, the zero is replaced by a single dot)

$$\rho = |\Phi\rangle\langle\Phi| = \begin{pmatrix} \frac{1}{4} & \cdot & \cdot & \cdot & \frac{1}{4} & \cdot & \cdot & \cdot & \cdot & \frac{1}{4} & \cdot & \cdot & \cdot & \cdot & \frac{1}{4} \\ \cdot & \cdot \\ \cdot & \cdot \\ \cdot & \cdot \\ \frac{1}{4} & \cdot & \cdot & \cdot & \frac{1}{4} & \cdot & \cdot & \cdot & \cdot & \frac{1}{4} & \cdot & \cdot & \cdot & \cdot & \frac{1}{4} \\ \cdot & \cdot \\ \cdot & \cdot \\ \cdot & \cdot \\ \frac{1}{4} & \cdot & \cdot & \cdot & \frac{1}{4} & \cdot & \cdot & \cdot & \cdot & \frac{1}{4} & \cdot & \cdot & \cdot & \cdot & \frac{1}{4} \\ \cdot & \cdot \\ \cdot & \cdot \\ \cdot & \cdot \\ \frac{1}{4} & \cdot & \cdot & \cdot & \frac{1}{4} & \cdot & \cdot & \cdot & \cdot & \frac{1}{4} & \cdot & \cdot & \cdot & \cdot & \frac{1}{4} \end{pmatrix}.$$

Referring to the CGLMP expression in Eq. 2.6, we consider $d = 4$ and this expression is written as

$$\begin{aligned} I_{2244}(\text{QM}) &= \sum_{k=1}^3 \sum_{l=1}^{4-k} P_{AB}^{kl}(1, 1) + \sum_{k=1}^3 \sum_{l=4-k}^3 [P_{AB}^{kl}(1, 2) + P_{AB}^{kl}(2, 1) - \\ & P_{AB}^{kl}(2, 2)] - \sum_{k=1}^3 P_A^k(1) - \sum_{l=1}^3 P_B^l(1) \\ &= P_{AB}^{11}(1, 1) + P_{AB}^{12}(1, 1) + P_{AB}^{13}(1, 1) + P_{AB}^{21}(1, 1) \\ & + P_{AB}^{22}(1, 1) + P_{AB}^{31}(1, 1) + P_{AB}^{13}(1, 2) + P_{AB}^{22}(1, 2) \\ & + P_{AB}^{23}(1, 2) + P_{AB}^{31}(1, 2) + P_{AB}^{32}(1, 2) + P_{AB}^{33}(1, 2) \\ & + P_{AB}^{13}(2, 1) + P_{AB}^{22}(2, 1) + P_{AB}^{23}(2, 1) + P_{AB}^{31}(2, 1) \\ & + P_{AB}^{32}(2, 1) + P_{AB}^{33}(2, 1) - P_{AB}^{13}(2, 2) - P_{AB}^{22}(2, 2) \\ & - P_{AB}^{23}(2, 2) - P_{AB}^{31}(2, 2) - P_{AB}^{32}(2, 2) - P_{AB}^{33}(2, 2) \\ & - P_A^1(1) - P_A^2(1) - P_A^3(1) - P_B^1(1) - P_B^2(1) - P_B^3(1). \end{aligned} \tag{2.12}$$

For simplicity, we write the coefficients of the joint probability in a compact manner via Table 2.2 with each of the entries representing the coefficient

2.2 Bell Inequalities

of the joint probability. There are 24 joint probabilities shown in the table.

Table 2.2: Coefficients of the joint probabilities.

	$P_B^1(1)$	$P_B^2(1)$	$P_B^3(1)$	$P_B^4(1)$	$P_B^1(2)$	$P_B^2(2)$	$P_B^3(2)$	$P_B^4(2)$
$P_A^1(1)$	1	1	1	.	.	.	1	.
$P_A^2(1)$	1	1	.	.	.	1	1	.
$P_A^3(1)$	1	.	.	.	1	1	1	.
$P_A^4(1)$
$P_A^1(2)$.	.	1	.	.	.	-1	.
$P_A^2(2)$.	1	1	.	.	-1	-1	.
$P_A^3(2)$	1	1	1	.	-1	-1	-1	.
$P_A^4(2)$

Table 2.3: Coefficients of all the probabilities with swapping of Bob's outcome.

	-1	-1	-1
-1	1	1	1	.	1	.	.	.
-1	.	1	1	.	1	1	.	.
-1	.	.	1	.	1	1	1	.
.
.	1	.	.	.	-1	.	.	.
.	1	1	.	.	-1	-1	.	.
.	1	1	1	.	-1	-1	-1	.
.

We then perform a swap of Bob's outcomes shown in Table 2.3 with -1 representing the coefficient of the probability of P_A^k or P_B^l shown in Eq. 2.12. The six additional terms, namely $P_A^1(1)$, $P_A^2(1)$, $P_A^3(1)$, $P_B^1(1)$, $P_B^2(1)$ and

2. THEORETICAL BACKGROUND

Table 2.4: Coefficients of all the probabilities with added joint probabilities $P_{AB}^{14}(1, 1)$, $P_{AB}^{24}(1, 1)$, $P_{AB}^{34}(1, 1)$, $P_{AB}^{44}(1, 1)$, $P_{AB}^{41}(1, 2)$, $P_{AB}^{42}(1, 2)$, $P_{AB}^{43}(1, 2)$ and $P_{AB}^{44}(1, 2)$.

	-1	-1	-1	-1
-1	1	1	1	1	1	.	.	.
-1	.	1	1	1	1	1	.	.
-1	.	.	1	1	1	1	1	.
-1	.	.	.	1	1	1	1	1
.	1	.	.	.	-1	.	.	.
.	1	1	.	.	-1	-1	.	.
.	1	1	1	.	-1	-1	-1	.
.

$P_B^3(1)$ are practically impossible to measure. As an example, with the condition $P_{AB}^{14}(1, 1) + P_{AB}^{24}(1, 1) + P_{AB}^{34}(1, 1) + P_{AB}^{44}(1, 1) - P_B^4(1) = 0$, we added the coefficients of this condition into Table 2.4 [50].

The coefficients of the non-joint probabilities in the Table 2.4 are taken care by the conditions, $-P_A^1(1) - P_A^2(1) - P_A^3(1) - P_A^4(1) = 1$ and $-P_B^1(1) - P_B^2(1) - P_B^3(1) - P_B^4(1) = 1$. Therefore these probabilities need not be measured in the experiment. The CGLMP inequality thus requires a minimum of 32 joint probabilities to be measured. Finally, for a 4-dimensional maximally-entangled state, the maximum violation of the CGLMP is evaluated to be $I_{2244}^{\max}(\text{QM}) = 0.33609$.

Chapter 3

Generation of Entangled Photon Pairs

We briefly describe the theory of spontaneous parametric down-conversion (SPDC) to generate polarization-entangled photon pairs. This is followed by a description of how to prepare energy-time entangled photons by introducing unbalanced Mach-Zehnder interferometers in the path of the photon pairs. In Section 3.4, we show how we can prepare polarization and energy-time entangled photons by placing interferometers into the signal and idler paths of the polarization-entangled photons from SPDC.

3.1 Entangled Photon Pairs

This section covers the theory of spontaneous parametric down-conversion (SPDC). This process is ideal for creating a high quality entangled state. The photonic qubit can be conveniently encoded in any of several degrees of freedom, namely polarization, energy-time, time-bin, and orbital angular momentum. One of the advantages of choosing photonic qubits is they can travel long distance without severe decoherence in the polarization. They are also easier to manipulate and detect since these techniques require classical optics which have been studied in detail. The theory of SPDC was established by Klyshko [51] in 1970 and the modern quantum mechanical description was provided by Hong [52] in 1985.

3. GENERATION OF ENTANGLED PHOTON PAIRS

3.1.1 Second-Order Non-linear Optical Phenomena

To understand the concept of the second-order non-linear optical phenomena, we begin by looking at the behaviour of the electrons and positively charged nuclei of the atoms in a dielectric material when subjected to an electric field of a light wave. When a dielectric material is subjected to an electric field \mathbf{E} , the electrons and positively charged nuclei of the atoms get polarized since the electric field redistributes the charges within the atoms. The sum of the induced electric dipole moments is written as

$$P_i = \epsilon_0 \chi_{ij}^{(1)} E_j + \epsilon_0 \chi_{ijk}^{(2)} E_j E_k + \dots + \epsilon_0 \chi_{ijk\dots l}^{(n)} E_j E_k \dots E_l, \quad (3.1)$$

where ϵ_0 is the electric permittivity of free space, χ is the linear electric susceptibility, E is the applied electric field, $i, j, \dots, k \in (1, 2, 3)$, and $\chi^{(n)}$ is the n th-order susceptibility. The susceptibility χ is related to the refractive index of the dielectric material. For an isotropic medium, the susceptibility χ only has one value which describes the refraction or dispersion characteristics of the electric field in the dielectric medium. For a crystalline material, the susceptibility χ is a tensor quantity related to the symmetry of the crystal structure. The spontaneous parametric down-conversion (SPDC) process is attributed to the non-linear coupling term, $\chi^{(2)}$ which is known as a second order non-linear interaction.

SPDC is stimulated by random vacuum fluctuations and the photon pairs are created at random times. Although the conversion efficiency is very low, it has been proven to be one of the most efficient methods to generate the entangled photon pairs. During the process of SPDC, a pump photon of frequency ω_p is annihilated thus producing a signal and idler photon at frequency ω_s and ω_i respectively, while satisfying the conservation of energy and momentum. The conservation laws [53] are written as,

$$\omega_p = \omega_s + \omega_i, \quad (3.2)$$

$$\vec{k}_p = \vec{k}_s + \vec{k}_i, \quad (3.3)$$

where Eq. 3.2 and Eq. 3.3 are known as the energy conservation and phase matching condition respectively. The phase matching is perfect for infinite crystal lengths and ideally planar pump electric waves.

As an illustration of β -Barium-Borate (BBO) crystal in our experiment, where there are two different refractive indices n_o and n_e for the ordinar-

3.2 Generation of Polarization-Entangled Photon Pairs

ily (o) and extraordinarily (e) polarized light respectively. This crystal is negative uniaxial since $n_x = n_y = n_o$, $n_z = n_e$ in the principal coordinate system and $n_e < n_o$. This crystal has been proven to produce a high-intensity source of polarization-entangled photon pairs [15].

The successive implementations of quantum protocols using polarization-entangled photon pairs generated from the BBO crystal have gained increased attentions among the researchers. The investigations of the properties of BBO crystal using theoretical models have been developed to study the spectra, emission time distribution and spatial emission distribution of the down-converted photons, see [54] and references therein. Experimental techniques have been developed to increase the generation of down-converted photon pairs into single mode fibers [55, 56, 57, 58]. These techniques are essential in the implementation of quantum protocols, i.e. long distance quantum key distribution [59, 60].

3.2 Generation of Polarization-Entangled Photon Pairs

The birefringence of the BBO crystal has to be considered for photons propagating in the crystalline medium. The emission direction of the signal and idler photons are specified by the angle between the pump photon wave vector and the optical axis of the crystal. There are two of types of phase matching, type-I and type-II, differentiated by whether the signal and idler photon within each pair have the same or orthogonal polarization. For a type-I process, the pump photon is extraordinarily-polarized (e -polarized) and both down-converted photons have the same polarization (o -polarized). For a type-II process, the pump photon is e -polarized. However, the polarizations of both down-converted photons are orthogonal.

In a type-II down-conversion process, the o and e -polarized photons are emitted from the down-conversion crystal in two cones which are non-concentric with either the pump beam or each other. In our setup, the down-conversion crystal is oriented in such a way that the extraordinary

3. GENERATION OF ENTANGLED PHOTON PAIRS

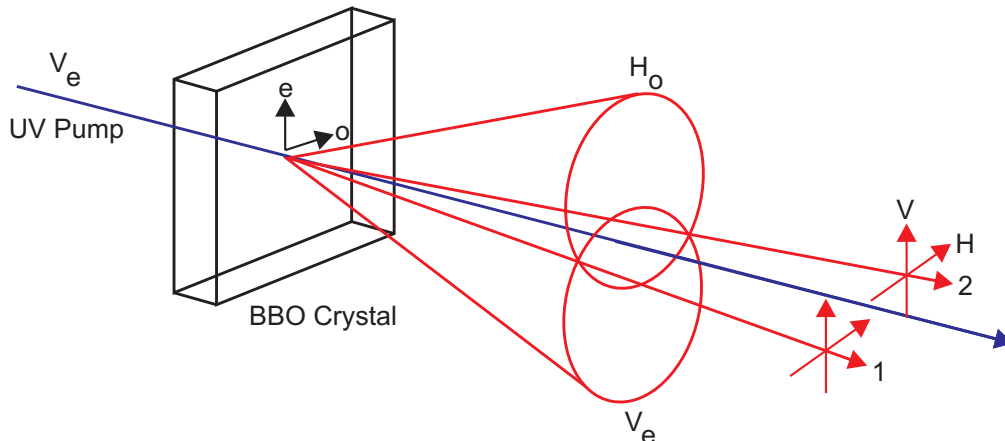


Figure 3.1: Type-II phase matched down-conversion [15]. In type-II phase matching, an e -polarized pump photon gets down-converted into a pair of o and e -polarized photons of lower energy. The o and e -polarized photons are emitted from the down-conversion crystal in two respective cones which are non-concentric with either the pump beam or each other. In our setup, the down-conversion crystal is oriented in such a way that the extraordinary axis coincides with the vertical (V) polarization, while the ordinary axis coincides with the horizontal (H) polarization. These two cases are denoted as V_e and H_o , respectively.

axis coincides with the vertical (V) polarization, while the ordinary axis coincides with the horizontal (H) polarization (Fig. 3.1) as proposed in [15]. By tilting the optical axis of the BBO crystal with respect to the pump wave vector, the emission cones of the down-conversion photons can be made to intersect. The photons detected at the intersections of the cones are indistinguishable in their wavelengths except for their polarizations. The polarized-entangled state is written as,

$$|\Psi\rangle_p = \frac{1}{\sqrt{2}} (|H_o\rangle_1 |V_e\rangle_2 + e^{i\delta} |V_e\rangle_1 |H_o\rangle_2), \quad (3.4)$$

with a relative phase δ between the H_e and V_o photons in each spatial mode.

3.2.1 Longitudinal and Transverse Walk-Off

In practice, down-converted photon pairs generated from the BBO crystal are not perfectly indistinguishable because the photon pairs propagate with different velocities inside the crystal. The different refractive index n_o and n_e of the birefringent crystal gives rise to a relative delay between the arrival time of the o and e -polarized photon in each pair that is dependent on the location where they are created in the crystal. This effect is called longitudinal walk-off and it reduces the time indistinguishability between the o and e -polarized photons [15]. The transverse walk-off is due to the reduced spatial mode overlap between the spatial profile distribution of the o and e -polarized photons [61].

3.2.1.1 Compensation of Longitudinal (Temporal) Walk-Off

If the photon pairs are created at the crystal location d with respect to the surface of the crystal facing to the pump beam, the time difference between the arrival time of the o and e -polarized photon is $\delta t = (L - d)\frac{(n_o - n_e)}{c}$, where c is the speed of light in the vacuum. The photon pairs created at the face of the crystal incident to the pump beam or $d = 0$ have maximum time difference while photon pairs created at the exit face of the crystal or $d = L$ have no time difference. The time difference is larger than the coherence time of the photon pairs $t_c \approx 100$ fs even with a thin crystal of millimeter length.

To eliminate this problem, a combination of half-wave plates ($\lambda/2$) and BBO compensation crystals (CC) is placed after the BBO pump crystal (Fig. 3.2) [15]. The photons first pass through $\lambda/2$ waveplate which rotates their polarization by 90° . This is followed by a CC whose optical axis (OA) is aligned in the same direction as the pump crystal. The CC halves the relative delay between the photons pairs and the final time difference is equal for the photon pairs generated at the surface and exit of the crystal. Therefore, the photons pairs from these two cases are indistinguishable in the temporal degree of freedom, resulting in a pure polarization-entangled state. This indistinguishability also holds for emission points at different locations of the crystal.

3. GENERATION OF ENTANGLED PHOTON PAIRS

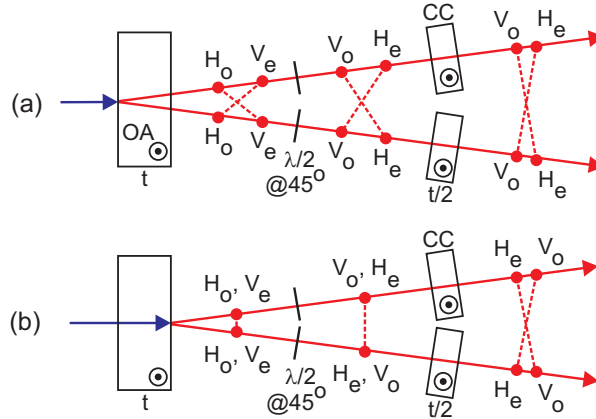


Figure 3.2: Compensation of temporal walkoff [62]. The photon pairs pass through a $\lambda/2$ waveplates in which their polarization is rotated by 90° . They then pass through compensation crystals (CC) which are identical to the crystal used for down-conversion except half of the thickness. In the first extreme case (a), the CC halves the relative delay between the photons in the pair. In the second extreme case (b), the CC induces a relative delay equal to that in the previous case between the photons in the pair. Hence, the photons pairs from these two cases are indistinguishable in the temporal degree of freedom, resulting in a pure polarization-entangled state.

3.2.1.2 Compensation of Transverse (Spatial) Walk-Off

At the intersection of the emission cones, there is an elongated spread of the o -polarized photon distribution as compared to the e -polarized photons (Fig. 3.3) [61]. The propagation direction of the pump photon energy flux, described by the Poynting vector is shifted with respect to the energy flux of the o -polarized photons but is equal to the e -polarized photons. Thus, o -polarized photons emitted will add up to an elliptical mode. Therefore, the axis in which the o -polarized photon emitted is shifted from the center with respect to the mode of the e -polarized photon. The shift is in the range of several tens of μm per mm of crystal length and hence reduces the mode overlap between the photon pairs. This causes an imbalance in the collection of both modes.

To eliminate this problem, the compensation scheme of temporal walk-

3.2 Generation of Polarization-Entangled Photon Pairs

off is used to compensate the transverse walk-off. The polarization of the photons are rotated by 90° after passing through the $\lambda/2$ waveplates. The CC causes a shift in the path of the down-converted light such that the center of the distribution of the o and e -polarized photons coincide. This provides better overlap between the two mode distributions and thus results in a better spatial mode for collection. In practice, we observed a difference in the number of o and e -polarized photons collected into the single mode fiber (SMF) with thick crystals. The reason is that the matching of the spatial mode profiles of the o and e -polarized photons decreases with increasing crystal length even if both modes are centered.

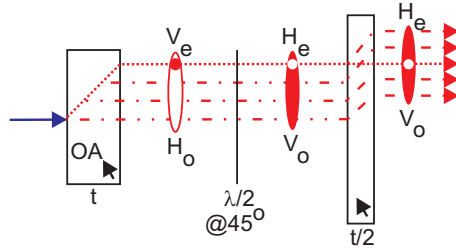


Figure 3.3: Compensation of transverse walkoff [62]. The polarization of the photon pairs after passing through the $\lambda/2$ is rotated by 90° . The compensation crystal (CC) causes a shift in the path such that the center of the distribution of the o and e -polarized photons coincide. This provides better overlap between the two distributions and thus results in a better spatial mode for collection.

Tilting the vertical angle between the fast axis of the CC and the down-converted light beam changes the relative phase between the H_e and V_o photons in each of the spatial modes. This allows the free phase δ (Eq. 3.4) to be adjusted such that different types of entangled states can be generated.

3. GENERATION OF ENTANGLED PHOTON PAIRS

3.2.2 Characterization of Polarization-Entangled Photon Pairs

Quantum state tomography [63, 64, 65, 66] provides full characterization of any quantum states by a joint measurement of the down-converted photons in various polarization bases. Instead of performing a full tomography in this work, joint detection measurement in selected polarization bases is sufficient to measure the quality of entanglement.

The joint detection probabilities of measurements involve the projection of the photon pairs onto linear polarization bases. This is implemented by inserting a polarization analyzer consisting of a rotatable $\lambda/2$ waveplate followed by a polarizing beam splitter (PBS), which transmits horizontal and reflects vertical polarization. The $\lambda/2$ waveplate does an unitary transformation or a rotation of angle α on the polarization of the photons which is given as

$$R(\alpha) = \begin{pmatrix} \cos \alpha & -\sin \alpha \\ \sin \alpha & \cos \alpha \end{pmatrix}. \quad (3.5)$$

The two single-photon basis polarization states $|H\rangle$ and $|V\rangle$ are given by the column vectors

$$|H\rangle = \begin{pmatrix} 1 \\ 0 \end{pmatrix}, |V\rangle = \begin{pmatrix} 0 \\ 1 \end{pmatrix}, \quad (3.6)$$

respectively.

For any arbitrary pure polarization state $|\psi\rangle$, the probability of detecting photons in a linear polarized basis at angle α from the horizontal axis $|H\rangle$ is written as

$$P(H|\alpha) = |\langle H|R(\alpha)|\psi\rangle|^2. \quad (3.7)$$

For photon pairs in the two polarization states, the rotation transformation matrix due to the two $\lambda/2$ waveplates is written as

$$R^{(2)}(\alpha, \beta) = R(\alpha) \otimes R(\beta), \quad (3.8)$$

where $R(\alpha)$ and $R(\beta)$ are the transformation performed in spatial mode 1 and 2 respectively. Therefore the joint detection probability of obtaining the measurement result $|H\rangle_1|H\rangle_2$ for the input state $|\Psi\rangle_p$ (Eq. 3.4) is given

3.3 Generation of Energy-time Entanglement

by

$$\begin{aligned} P(H, H|\alpha, \beta) &= |\langle H|_1 \langle H|_2 R(-\alpha, -\beta) |\Psi\rangle_p|^2 \\ &= \frac{1}{2} \sin^2(\alpha - \beta). \end{aligned} \quad (3.9)$$

when $\delta = \pi$.

The visibility of the joint detection measurement in the H/V and $+45^\circ/-45^\circ$ bases are related to the quality of polarization entanglement. For $\delta = \pi$ in the input state $|\Psi\rangle_p$ (Eq. 3.4), the entangled state is

$$|\Psi^-\rangle = \frac{1}{\sqrt{2}} (|H\rangle_1 |V\rangle_2 - |V\rangle_1 |H\rangle_2). \quad (3.10)$$

The $|\Psi^-\rangle$ state is rotationally invariant, it is left unchanged by a coordinate transformation performed on the $+45^\circ/-45^\circ$ basis, i.e.

$$|\Psi^-\rangle = \frac{1}{\sqrt{2}} (|+\rangle_1 |-\rangle_2 - |-\rangle_1 |+\rangle_2), \quad (3.11)$$

where $+$ and $-$ denote the $+45^\circ$ and -45° polarization basis respectively.

The definition of the visibilities measured in the H/V and $+45^\circ/-45^\circ$ bases, denoted as V_{HV} and V_{+-} respectively, can be written as

$$V_{HV} = \frac{|C_{VH} - C_{VV}|}{C_{VH} + C_{VV}}, \quad (3.12)$$

$$V_{+-} = \frac{|C_{+-} - C_{++}|}{C_{+-} + C_{++}}, \quad (3.13)$$

where C_{ij} is the number of coincidences obtained when the down-converted photons in spatial mode 1 and 2 are projected onto polarization i and j respectively. For the $|\Psi^-\rangle$ states in Eq. 3.10 and Eq. 3.11, both quantities V_{HV} and V_{+-} will have the value of 1 as there are no contributions giving rise to coincidences C_{VV} or C_{++} .

By varying the angle α or β of the $\lambda/2$ waveplates, the C_{ij} is measured and hence the visibility can be computed which gives a measure of the quality of the polarization-entangled photon pairs.

3.3 Generation of Energy-time Entanglement

In 1990, Ou *et. al.* demonstrated energy-time entanglement successfully using photon pairs generated from SPDC [17]. The original idea came from

3. GENERATION OF ENTANGLED PHOTON PAIRS

an experiment proposed by Franson in 1989 to prepare an energy-time entangled state using three level atoms with unbalanced Mach-Zehnder interferometers on each of the photon paths [67]. In the SPDC demonstration (Fig. 3.4), the first condition is that the interferometer path length difference has to be chosen such that the implemented time delay ΔT is much longer than the coherence time of the down-conversion photon pairs τ_1 . This condition avoids single photon interference. Typically the photon pairs are detected within a bandwidth of few nanometers, or coherence time of around 100 fs. The second condition is that the delay ΔT must be smaller than the coherence time of the pump photon τ_2 . This condition guarantees the coherent superposition of the photon pairs which take the short path $|0\rangle$ or long path $|1\rangle$ in the interferometers, see Fig. 3.4. The third condition is that ΔT must be long enough to discard and postselect events occurring when one photon takes the short path and the other takes the long path and vice versa. This requirement implies that the coincidence time window of the photon pair detection must be shorter than the delay ΔT in order to discard photon pairs taking the short path and the other taking the long path and vice versa as well. In other words, by choosing an appropriate coincidence time window, we can postselect the both photon pairs taking the short-short path and long-long path, see Fig. 3.5. To sum up, these three conditions impose $\tau_2 > \Delta T > \tau_1$ which must be satisfied in the experiment.

The coincidences between the photon pairs are detected at three possible detection time windows (Fig. 3.5), namely $(-\Delta T, 0, \Delta T)$. There are four possible combinations for coincidence detection, namely $|0\rangle_A|0\rangle_B$, $|1\rangle_A|1\rangle_B$, $|0\rangle_A|1\rangle_B$, and $|1\rangle_A|0\rangle_B$. The states $|0\rangle_A|0\rangle_B$ and $|1\rangle_A|1\rangle_B$ are indistinguishable since the time delay in the coincidence measurement detection for these states are zero. The coincidence time window is shorter than ΔT in order to postselect the indistinguishable states $|0\rangle_A|0\rangle_B$ and $|1\rangle_A|1\rangle_B$. The entangled state is written as the coherent superposition of these indistinguishable states

$$|\Phi\rangle_t = \frac{1}{\sqrt{2}} (|0\rangle_A|0\rangle_B - e^{i(\phi_A+\phi_B)}|1\rangle_A|1\rangle_B), \quad (3.14)$$

with $\phi_{A,B}$ being the phase differences between the long and short paths in the interferometers respectively. The phase $\phi_{A,B}$ is adjusted such that

3.3 Generation of Energy-time Entanglement

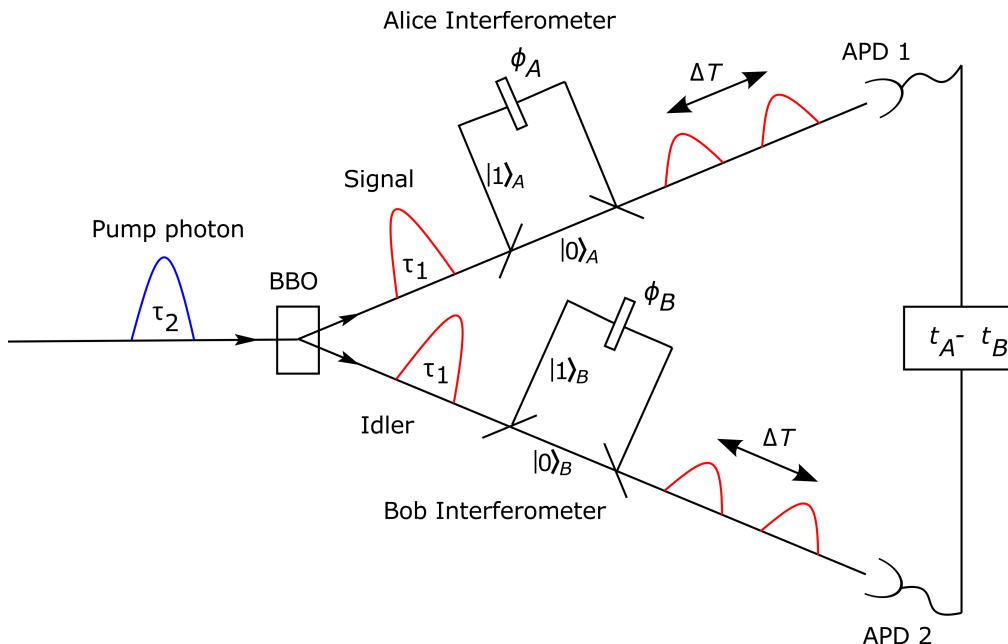


Figure 3.4: Experimental setup for energy-time entanglement. A pump photon with coherence time τ_2 is down-converted into correlated photon pairs with coherence time τ_1 . The photon pairs are sent into Mach-Zehnder interferometers which introduces a time delay ΔT due to the unbalanced arm lengths (short path $|0\rangle$ and long path $|1\rangle$). The condition $\Delta T < \tau_2$ guarantees the coherent superposition of the photon pairs which take the short path $|0\rangle$ or long path $|1\rangle$ in the interferometers. The Franson interference [67] or second order correlation between the photon pairs are measured by silicon avalanche photodiodes (APD), with a time delay $t_A - t_B$ between APD 1 and APD 2.

different entangled states can be generated, with a condition that the phase difference $\phi_{A,B}$ is kept equal up to the coherence time of the down-converted photons τ_1 .

3.3.1 Time-bin Entanglement

In time-bin entanglement [20, 21], the entangled photon pairs have well defined emission times instead of being undetermined over the long coherence

3. GENERATION OF ENTANGLED PHOTON PAIRS

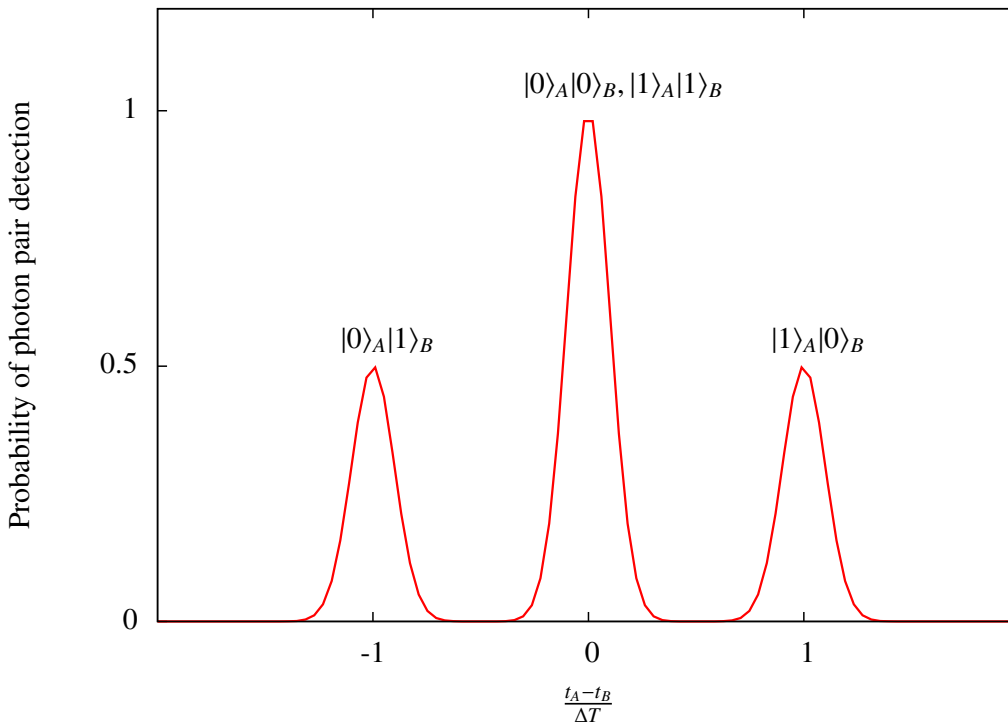


Figure 3.5: Four possible amplitudes of the photon pairs in the time delay basis. The two coherent states $|0\rangle_A|0\rangle_B$ and $|1\rangle_A|1\rangle_B$ overlap up to the coherence time of the down-converted photon pairs τ_1 and there is no single photon interference under the condition where the coherence time of the down-converted photons are less than the time delay introduced by the unbalanced Mach-Zehnder interferometer, $\tau_1 < \Delta T$.

time of the pump photon τ_2 . This can be implemented by using a femtosecond pulsed laser whereby the emission time is well defined. However, the pulse train from a mode-locked laser can have a broad overall bandwidth and the pulses are not coherent to each other. Thus, the coherence time $\tau_2 > \Delta T$ cannot be fulfilled. Introducing an additional unbalanced Mach-Zehnder interferometer in the pump beam splits the pulse train into a fixed delay ΔT . Thus, the successive pulses are now indistinguishable from the preceding pulses and the states of the photon pairs $|0\rangle_A|0\rangle_B$ and $|1\rangle_A|1\rangle_B$ generated from SPDC are indistinguishable. In short, the path indistinguishability between the path $|0\rangle_{\text{pump}}|1\rangle_{A,B}$ and $|1\rangle_{\text{pump}}|0\rangle_{A,B}$ leads to a time-bin entangled state after postselection. Since the work in this thesis

does not employ a pulsed laser, the theory of the time-bin entanglement will not be presented here. More details can be found in [20, 21].

3.3.2 Characterization of Energy-time Entangled Photon Pairs

The quality of energy-time correlation is determined by measuring the joint detection probability of the photon pairs, also known as Franson interference. We simplify the mathematical explanation of the Franson interference in the original paper [67]. The state of mode 1 and mode 2 are written as

$$\psi(\mathbf{r}_{1,2}, t) = \frac{1}{2}\psi_0(\mathbf{r}_{1,2}, t) + \frac{1}{2}e^{i\phi_{A,B}}\psi_0(\mathbf{r}_{1,2}, t - \Delta T) \quad (3.15)$$

The coincidence function R between APD 1 and APD 2 is

$$R = \langle 0 | \psi^\dagger(\mathbf{r}_1, t) \psi^\dagger(\mathbf{r}_2, t) \psi(\mathbf{r}_1, t) \psi(\mathbf{r}_2, t) | 0 \rangle. \quad (3.16)$$

We are interested in the event in which both down-converted photons take the short path and long path. The above expression is thus simplified as

$$R = \frac{1}{16} \langle 0 | [\psi_0^\dagger(\mathbf{r}_1, t) \psi_0^\dagger(\mathbf{r}_2, t) + e^{-i(\phi_A + \phi_B)} \psi_0^\dagger(\mathbf{r}_1, t - \Delta T) \psi_0^\dagger(\mathbf{r}_2, t - \Delta T)] \times [\psi_0(\mathbf{r}_1, t) \psi_0(\mathbf{r}_2, t) + e^{i(\phi_A + \phi_B)} \psi_0(\mathbf{r}_1, t - \Delta T) \psi_0(\mathbf{r}_2, t - \Delta T)] | 0 \rangle. \quad (3.17)$$

The conservation of energy from the pump frequency ω_p to final states $\omega_{s,i}$ requires that

$$\omega_p + \Delta\omega = \omega_s + \omega_i, \quad (3.18)$$

where $\Delta\omega$ is the uncertainty of the pump frequency. We write

$$\psi_0(\mathbf{r}_1, t - \Delta T) \psi_0(\mathbf{r}_2, t - \Delta T) = e^{i(\omega_p + \Delta\omega)\Delta T} \psi_0(\mathbf{r}_1, t) \psi_0(\mathbf{r}_2, t). \quad (3.19)$$

Assuming $\Delta\omega\Delta T \ll 1$ and neglecting the contribution from this term, thus the coincidence function can be written as

$$\begin{aligned} R &\propto [1 + e^{-i(\omega_p\Delta T + \phi_A + \phi_B)}][1 + e^{i(\omega_p\Delta T + \phi_A + \phi_B)}] \\ &\propto \cos^2\left(\frac{\omega_p\Delta T + \phi_A + \phi_B}{2}\right). \end{aligned} \quad (3.20)$$

3. GENERATION OF ENTANGLED PHOTON PAIRS

The coincidence function depends on the sum of the relative phases and a constant offset given by the frequency of the pump photon ω_p . The visibility of this coincidence function measures the quality of the correlation if R varies between 0 and 1. In practice, the reduction of this visibility is due to the ratio between the difference in path length difference in both interferometers, δ to the finite coherence time of the photon pairs τ_1 [68]. As such, the visibility can be written as

$$R = \cos^2\left(\frac{\phi_A + \phi_B + \omega_p \Delta T}{2}\right) e^{-\left(\frac{\delta}{c\tau_1}\right)^2}. \quad (3.21)$$

Thus, in order to maintain high visibility, this δ should be kept minimum with respect to the interferometers.

3.4 Entanglement in a High-Dimensional Bipartite System

The polarization-entangled state is intrinsically 2 dimensional since only two linearly independent polarization vectors span the Hilbert space. One way of generating higher-dimensional polarization-entangled states is to replace the pump photon with repeated pump pulses emitted from a mode-locked femtosecond laser. The higher order emission of the SPDC photons generates multiphoton polarization-entangled states [69, 70]. As discussed in Section 3.1.1, the probability of obtaining higher order emission is low which leads to a low brightness of the multiphoton-entangled source [71]. Furthermore, the losses introduced by the optical elements and the efficiency of the photodiode lead to longer data acquisition times. The energy-time entangled state allows us to create entangled states with a higher dimension, $N > 2$ by implementing at least two or more interferometers in one arm in both spatial modes [72, 73, 74]. The dimension is therefore directly dependent upon the transformation by the interferometers and not limited by the intrinsic property of the polarization of photons which spans only 2-dimensional space. In practice, this provides a direct generation of higher dimensional entangled states but the implementation of this experimental scheme requires the stabilization of multiple interferometers. The

3.4 Entanglement in a High-Dimensional Bipartite System

other approach is to repeat the 2 dimensional time-bin entanglement by using repeated pump pulses [75], but a full analysis of the state is not trivial. Higher dimensional entanglement can also be realised for the orbital angular momentum degree of freedom [76, 77, 78, 79, 80]. Although most of these experiments exhibit non-classical behaviour, the definition of the dimension witness is insensitive to whether our system is quantum or classical.

In this thesis, we generate higher dimensional states entangled in multiple degrees of freedom also known as a hyperentangled state [71, 81, 82]. A hyperentangled state $|\text{HE}\rangle$ can be defined as follows,

$$|\text{HE}\rangle = |\text{Bell}\rangle_1 \otimes |\text{Bell}\rangle_2 \otimes |\text{Bell}\rangle_3 \dots \quad (3.22)$$

where each term corresponds to one of the four Bell states encoded in one of the degrees of freedom of two particles. Bell states represent the simplest examples of two qubit entangled states and they are expressed as,

$$|\Phi^\pm\rangle = \frac{1}{\sqrt{2}} (|0\rangle_A |0\rangle_B \pm |1\rangle_A |1\rangle_B), \quad (3.23)$$

$$|\Psi^\pm\rangle = \frac{1}{\sqrt{2}} (|0\rangle_A |1\rangle_B \pm |1\rangle_A |0\rangle_B). \quad (3.24)$$

Hyperentangled states allow improvement in super dense coding [83], full Bell-state analysis [84, 85, 86, 87], simplification of quantum logic [88], remote entangled state preparation [89] and enhancing the quantum non-locality tests [90].

We introduce the energy-time entanglement to photon pairs which are entangled in polarization. The photon pairs entangled in polarization and energy-time leads to a 4 dimensional entangled state. The state after the coincidence time window postselection is

$$\begin{aligned} |\Phi\rangle &= |\phi_{\text{polarization}}^+\rangle \otimes |\phi_{\text{energy-time}}^+\rangle \quad (3.25) \\ &= \frac{1}{\sqrt{2}} (|H\rangle_A |H\rangle_B + |V\rangle_A |V\rangle_B) \otimes \frac{1}{\sqrt{2}} (|s\rangle_A |s\rangle_B + |l\rangle_A |l\rangle_B) \\ &= \frac{1}{2} (|Hs\rangle_A |Hs\rangle_B + |Vs\rangle_A |Vs\rangle_B + |Vl\rangle_A |Vl\rangle_B + |Hl\rangle_A |Hl\rangle_B). \end{aligned}$$

Denoting the polarization degree of freedom $|H\rangle = \begin{pmatrix} 1 \\ 0 \end{pmatrix}$, $|V\rangle = \begin{pmatrix} 0 \\ 1 \end{pmatrix}$ and energy-time degree of freedom $|s\rangle = \begin{pmatrix} 1 \\ 0 \end{pmatrix}$, $|l\rangle = \begin{pmatrix} 0 \\ 1 \end{pmatrix}$, it can be

3. GENERATION OF ENTANGLED PHOTON PAIRS

shown

$$|Hs\rangle = |H\rangle \otimes |s\rangle = \begin{pmatrix} 1 \\ 0 \end{pmatrix} \otimes \begin{pmatrix} 1 \\ 0 \end{pmatrix} = \begin{pmatrix} 1 \\ 0 \\ 0 \\ 0 \end{pmatrix} = |0\rangle \quad (3.26)$$

$$|Vs\rangle = |V\rangle \otimes |s\rangle = \begin{pmatrix} 0 \\ 1 \end{pmatrix} \otimes \begin{pmatrix} 1 \\ 0 \end{pmatrix} = \begin{pmatrix} 0 \\ 0 \\ 1 \\ 0 \end{pmatrix} = |1\rangle \quad (3.27)$$

$$|Vl\rangle = |V\rangle \otimes |l\rangle = \begin{pmatrix} 0 \\ 1 \end{pmatrix} \otimes \begin{pmatrix} 0 \\ 1 \end{pmatrix} = \begin{pmatrix} 0 \\ 0 \\ 0 \\ 1 \end{pmatrix} = |2\rangle \quad (3.28)$$

$$|Hl\rangle = |H\rangle \otimes |l\rangle = \begin{pmatrix} 1 \\ 0 \end{pmatrix} \otimes \begin{pmatrix} 0 \\ 1 \end{pmatrix} = \begin{pmatrix} 0 \\ 1 \\ 0 \\ 0 \end{pmatrix} = |3\rangle \quad (3.29)$$

The quantum state in Eq. 3.25 can be written as

$$|\Phi\rangle = \frac{1}{2} (|00\rangle + |11\rangle + |22\rangle + |33\rangle), \quad (3.30)$$

which spans the 4 dimensional Hilbert space.

In this experiment, we generate energy-time entanglement similar to that proposed in [17] to photon pairs which are entangled in polarization [15]. We measured the CGLMP inequality by carrying out two measurements on one party, A_1 or A_2 , and the other party, can also carry out two measurements, B_1 or B_2 . Each measurement has 4 possible outcomes: $A_1, A_2, B_1, B_2 = 0, 1, 2, 3$. In Chapter 5, we will explain the derivation of this 4-dimensional CGLMP inequality and experimental setup in detail.

Chapter 4

Implementation of Sources of 2-Dimensional Entangled Photon States

Photonic systems are one of the main workhorses for contemporary quantum research. They have various properties, *i.e.* polarization, linear momentum, and orbital angular momentum, which can serve as degrees of freedom by which quantum states can be encoded. The resistance of these properties and thus the quantum states they represent to decoherence, makes photons the ideal carriers of these quantum states.

Two or more photonic quantum states could exist in what are called entangled states. These entangled states describe the system of two or more photons as a whole and could not be derived from the individual quantum states of constituent photons. It is this quantum entanglement that makes it possible to, just to name a few, implement in principle totally secure encryption key distribution protocol [91], realize the teleportation of photonic quantum states [10] from one point to another, and allow us to factorize a large prime number [3] at a much higher speed than what current electronic computers are capable of.

For many decades and still up to today, the process of spontaneous parametric down-conversion (SPDC) in non-linear optical crystals is frequently employed to generate these entangled photons. The SPDC process

4. IMPLEMENTATION OF SOURCES OF 2-DIMENSIONAL ENTANGLED PHOTON STATES

is well understood and it offers a relatively simple way to experimentally implement a source of entangled photons [92]. Thus naturally we decided to go down the same route for the implementation of our entangled photon pair source.

In this Chapter, we start off by detailing the characterization of the various factors influencing the efficiency of our entangled photon pair source. We then describe the procedure for setting up a polarization and time-energy entangled photon pair source. We will also give an in depth functional description of the experimental setup and report on the result of the characterization of the efficiency of our source and the quality of the entangled state that was generated.

4.1 Photon Pairs Collection

In order to analyze the photon pairs from SPDC, they must first be collected. This is usually done by imaging each of the two down-converted photons from the down-conversion medium into two single mode optical fibers (SMF) by means of collection lenses. The lens and SMF combination provides us with a very well-defined and adjustable spatial mode for the collection of the down-converted photons.

As discussed in Section 3.1.1, SPDC is a spontaneous and weak process, hence the photon pairs are created at random times. In an idealized case, where the collection of the down-converted photons are perfect, every photon collected in one SMF corresponds to another photon in the other fiber. However, in practice, this is not the case due to a mismatch between the spatial mode of the collection and that of the down-converted light, and the inefficiencies of the detection instrumentation. To characterize this effect, we implemented the simplified photon pair source as shown in Fig. 4.1. The photon pairs are generated by SPDC using a β -barium borate (BBO) crystal. BBO crystals offer certain advantages compared to other non-linear crystals, i.e. wide optical transmission window from 190-3300 nm and high damage threshold, 500 MW/cm² in the UV region. The wavelength degeneracy of the photon pairs is independent of the temperature of the crystal, but depends on the cut of the crystal with respect

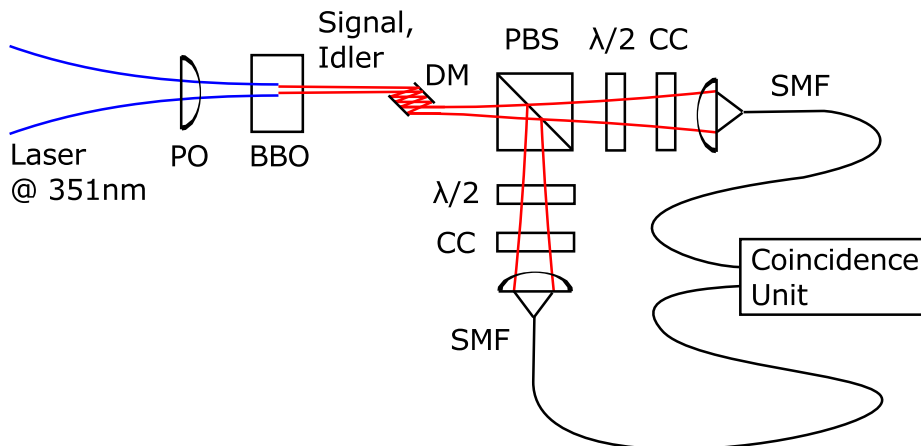


Figure 4.1: Schematic of the spontaneous parametric down-conversion (SPDC) setup. An Argon-ion cw-pumped SPDC process generates photon pairs in single mode optical fibers (SMF). Dichroic mirrors (DM) separate the 702 nm photon pairs from the residual 351 nm pump beam. The orthogonally polarized photon pairs generated by type-II SPDC are separated by a polarizing beam splitter (PBS).

to the propagation direction of the pump beam. Thus, this allows for the critical phase matching condition to be satisfied [93].

Fig. 4.1 shows a BBO crystal pumped by an Argon-ion laser (Coherent, Innova 300) with central wavelength, $\lambda_p = 351$ nm. The profile of the output beam TEM_{00} allows the spatial mode creation of the photon pairs to be optimally coupled into single mode optical fibers (SMF). This light passes through pump optics (PO) to focus the beam down to a waist of $89 \mu\text{m}$. At the focus, a l mm thick BBO crystal cut for collinear type-II phase matching ($\theta = 49.2^\circ$, $\phi = 30.0^\circ$) is placed. The crystal is tilted such that the emission direction of the photon pairs, $\lambda_{s,i} = 702$ nm is parallel to the pump beam. The photon pairs then pass through a few dichroic mirrors (DM), which transmit the pump beam with wavelength 351 nm and reflects the photon pairs of wavelength 702 nm. The signal and idler photon pairs which have orthogonal polarizations are separated by a polarizing beam splitter (PBS). The spatial modes of the photon pairs, defined by SMF, are matched to the pump mode to optimize the collection of the photon pairs [55, 56, 57, 58].

4. IMPLEMENTATION OF SOURCES OF 2-DIMENSIONAL ENTANGLED PHOTON STATES

The subsequent photon pairs are detected by silicon avalanche photodiodes (APD). The coincidences between the photon pairs are registered once the delay between the two arms are adjusted to compensate for electronic and optical path length differences. The collection efficiency is defined as [94],

$$\eta = \sqrt{\eta_1 \eta_2} \frac{\eta_l R_c}{\sqrt{R_1 R_2}},$$

where R_c is the coincidence count rate between the two detectors, R_1 and R_2 are the signal and idler single count rates, η_l is the optical loss after the crystal, which is due to the dichroic mirrors, coupling into single mode fibers and losses in the fibers. η_1 and η_2 are the APD detection efficiencies which are about 50% to 60%. We repeated this experiment for different crystal lengths $l = 1$ mm, 2 mm, and 10 mm to assess the collection efficiency of the down conversion source. The collection efficiencies using a tightly focused pump beam with a waist of $82 \mu\text{m}$ is 33.3% for a 1 mm crystal, 26.1 % for a 2 mm crystal and 16.6 % for a 10 mm crystal. We attributed the low efficiency of the setup to the four dichroic mirrors which introduces a loss of 15 %, this corresponds to a reflectivity of approximately 96% for each mirror.

The number of detected photon pairs scales as the square of the length of the crystal, l^2 [95]. However the angular width of the SPDC ring and bandwidth is proportional to $1/l$ while the useful intersecting area between the two rings scales as $1/l^2$. The number of photon pairs within this area (for a fixed spectral bandwidth) is independent of the crystal length. A thicker crystal would certainly produce a larger number of photon pairs with a narrower spectral bandwidth, however, the collection of these photon pairs into the SMF collection optics would be less. An infinitely thin crystal would give a perfect collection efficiency. This is in agreement what we observed in the experiment where the collection efficiency using a thin 2 mm crystal is higher than that of a 10 mm long crystal, see Fig 4.2. Thus, we adopt the 2 mm long crystal in our down-conversion source of photon pairs.

In addition, we observed a pronounced transverse walk-off with a 10 mm crystal which lowers the collection efficiency. As discussed in Section 3.2.1.2, compensation crystals (CCs) were used to compensate for the spatial walk-off such that the centre for the distribution of the o and e -polarized photon pairs coincide. There is still a relatively large spread in the spatial mode

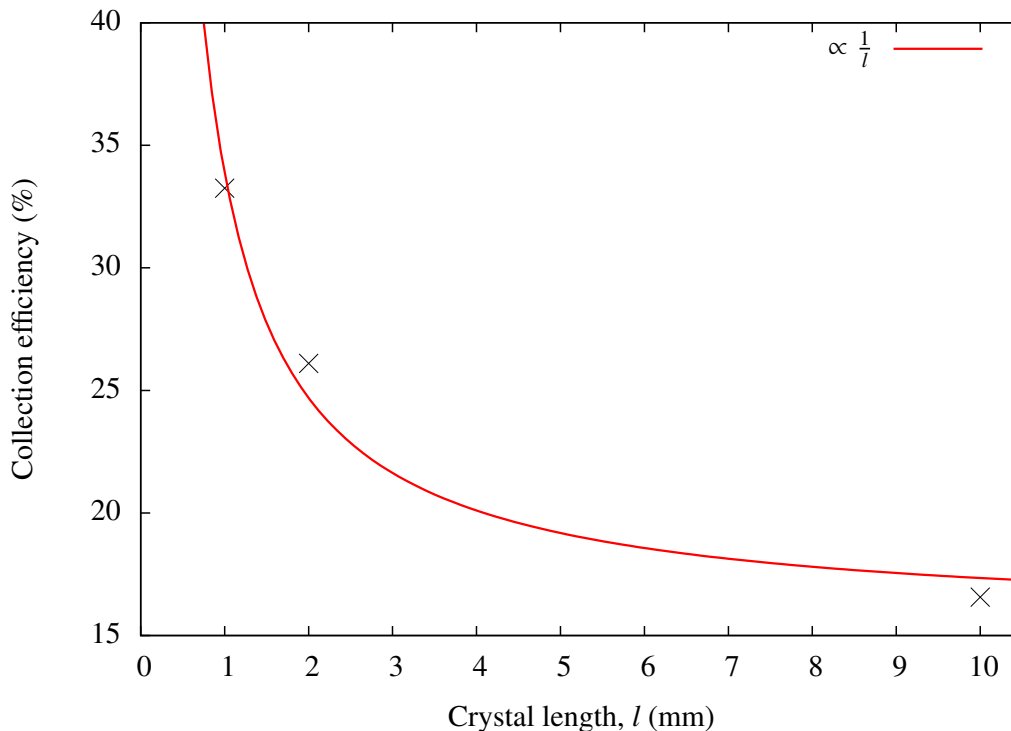


Figure 4.2: The collection efficiencies of the photon pairs generated via the SPDC process versus BBO crystal length. The collection efficiency using a tightly focused pump beam of waist $82\ \mu\text{m}$ is 33.3% for a 1 mm crystal, 26.1% for a 2 mm crystal and 16.6% for a 10 mm crystal. The observed collection efficiency increases with a thinner pump crystal. The curve is inversely proportional to the crystal length, l .

profile of the e -polarized photon compared to o -polarized photon. This reduces the spatial mode overlap between the o and e -polarized photon, hence the coupling of both modes into the SMF is lowered.

4.2 Characterization of Detector Efficiency

Once the down-converted photons are collected into SMFs, we require information on how well the down-converted photons are detected. A less than ideal detection of the photons would lead to differences between the measured and actual collection efficiency assuming completely efficient de-

4. IMPLEMENTATION OF SOURCES OF 2-DIMENSIONAL ENTANGLED PHOTON STATES

tection. Thus the efficiency of the detector has to be taken into account when we assess the collection efficiency of the photon pair source. It is important to note that the efficiency of a detector is actually a culmination of two influencing factors: how well the photons are coupled to the active detection area of the detector and the quantum efficiency of the active area. For the purpose of our characterization, it was not possible to distinguish between the two. Only a characterization of the overall detector efficiency is possible.

Quantum efficiency can be defined as the fraction of incident photons on the photodiode which contribute to the external photocurrent or photon counts. Photodiodes are semiconductor devices which contain a p-n junction and often an intrinsic (undoped) layer between the n and p layers [96]. Photons absorbed in the depletion region or the intrinsic region generate electron-hole pairs, most of which contribute to the photocurrent. A higher responsivity, defined as photocurrent per unit power of input light (AW^{-1}), can be achieved with avalanche photodiodes which are operated with a relatively high reverse bias voltage such that secondary electrons can be generated when the photodiode is operated in a Geiger mode. Silicon photodiodes offer quite high internal quantum efficiency at the mid and infra-red range, with the efficiency depending on the wavelength. Surface reflectivity of the silicon detection area, thickness of the silicon, and reverse bias voltage across the photodiode also affect the overall quantum efficiency.

We performed a simple experiment to estimate the detection efficiency of a silicon avalanche photodiode (APD). We prepared a collimated beam of wavelength λ , with a beam size of approximately 1 mm in diameter. The beam is subsequently split by a beam splitter (BS) into two paths. The transmitted beam is sent to a Hamamatsu (model: S1227-1010) photodetector (PD) with a 10 mm x 10 mm detection area which has been precalibrated for its responsivity. The photocurrent generated is measured using a high sensitivity digital ammeter (HP, model: 3458A). The reflected beam is sent to a set of neutral density filters which attenuates the light by an order of 10^{-14} before being detected by an APD (Perkin Elmer, model: C30902S) with a 0.2 mm^2 action detection area. We measured the detection efficiency of the APD by comparing the number of photons generated

4.2 Characterization of Detector Efficiency

from the photocurrent at the PD and the number of photons registered at APD.

The photon counts per second generated from the photocurrent I of the PD is

$$n_{\text{PD}} = \frac{I\lambda}{Ahc}, \quad (4.1)$$

where A is the sensitivity of the photodiode, h is Planck's constant, and c is the speed of light. From this we can calculate the detection efficiency of the APD given by,

$$\eta_{\text{APD}} = (n_{\text{APD}} - n_{\text{dark}})/n_{\text{PD}}, \quad (4.2)$$

where n_{APD} is the counts registered by the APD and n_{dark} is the dark count when the APD is not exposed to any light. The dark count increases with increasing reverse bias voltage and increasing in the temperature of the APD.

The accuracy of the APD detection efficiency characterization depends on the accuracy in characterizing the attenuation of each neutral density filter. We measured the attenuation by measuring the optical power of a beam, by means of a PD, before and after it passes through the neutral density filter. The optical power measurement is done by measuring the photocurrent output from the PD. The photocurrent is on the order of mA for 780 nm (output from a Ti:Sa laser, operated in cw mode) and becomes less than μA after the neutral density filters. The accuracy of the measurement of this weak photocurrent is up to nA. For the 632.8 nm output from a HeNe laser which is less bright compared to the Ti:Sa laser, the extremely weak photocurrent being measured contributes to a higher uncertainty of the attenuation measurement for each neutral density filter. Thus, the detection efficiency for the input wavelength at 630 nm has an uncertainty of 13.4% compared to 780 nm which has a lower uncertainty of only 0.8%.

The obtained detection efficiency of an APD with different input wavelengths are summarized in Table 4.1. The detection efficiency varies with different reverse bias voltages applied to the APD. A larger bias voltage increases the probability of breakdown, thus increasing the probability of photon detection and also increases the dark count.

4. IMPLEMENTATION OF SOURCES OF 2-DIMENSIONAL ENTANGLED PHOTON STATES

Table 4.1: Estimation of the detection efficiency η of the APD.

Laser source	$\lambda(\text{nm})$	$I(\text{mA})$	$A(\text{A/W})$	$\eta(\%)$	uncertainty in η (%)
HeNe	632.8	< 0.002	0.43	35.9	13.4
Ti:Sa (cw)	780	5.84	0.57	62.6	0.8

To summarize, in conjunction with the measurement result obtained in the previous section, the collection efficiency of the photon pairs in the experiment is greatly reduced by a factor of η . The collection efficiency of the source using a type-II 1 mm BBO is 33%, with a detection efficiency of approximately 60%. We note that it is possible to obtain higher collection efficiencies with type-I BBO crystals in a collinear configuration. This configuration utilized two adjacent BBO crystals (each 15.74 mm length) has reported a collection efficiency of 36-39%, with a detection efficiency around 51% [97].

4.3 Polarization-Entangled Photons

For the generation of polarization-entangled photons, we implement a typical down-conversion source similar to that proposed in [15]. Our setup is shown in Fig. 4.3. The BBO crystal is pumped continuously by a blue laser diode (Nichia, NDHV310APC, maximum output power of 60 mW) with a running wavelength of $\lambda_p = 405.1$ nm. The laser diode is mounted inside a collimation tube which is temperature stabilized by placing a peltier element under the diode mounting. For an external cavity diode laser (ECDL) configuration, an UV reflective holographic grating (Thorlabs, GH13-36U, 3600 lines per mm) is placed in front of the collimation tube (Thorlabs, C220-TMA, $f = 11$ mm). The purpose of this diffraction grating is to lengthen the free running coherence length of the diode laser from ≈ 1 mm to ≈ 1 m. As discussed in Section 3.3, the coherence length of the pump laser is one of the key features in order to generate the energy-time entanglement in the experiment discussed in Section 4.4. The diffraction grating is used as the wavelength-selective element in the external

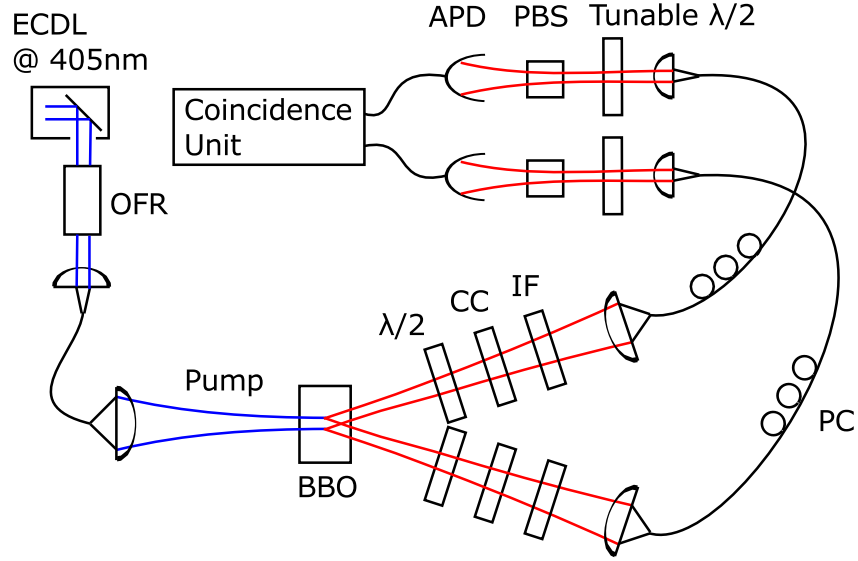


Figure 4.3: Schematic setup of a SPDC source of polarization-entangled photon pairs. An external cavity diode laser (ECDL) pumps a BBO crystal which generates polarization-entangled photon pairs via SPDC which are coupled into SMF. The down-converted signal and idler of photon pairs, wavelength $\lambda_{s,i} = 810$ nm emerge at an angle of approximately 3° from the axis of propagation of the residual 405 nm pump beam. The polarization correlation is measured by projecting the photon pairs onto linear polarization basis, which is selected by tunable $\lambda/2$ waveplates and polarizing beam splitters (PBS).

resonator. The first-order diffracted beam provides optical feedback to the laser diode and the emission wavelength can be tuned by rotating the diffraction grating. A disadvantage is that this also changes the direction of the output beam, which is inconvenient for many applications. An optical Faraday rotator (OFR, IO-5-405-LP) is placed after the grating to minimize the back reflection from the fiber coupling to the laser diode. The output of the fiber passes through an aspheric lens (Thorlabs, C220-TMA, $f = 11$ mm) in order to focus down the beam down to a waist of $80 \mu\text{m}$. At the focus, a 2 mm thick BBO crystal cut for type-II phase matching ($\theta = 42.3^\circ$, $\phi = 30.0^\circ$) is placed. The crystal is tilted such that the emission direction of the photon pairs, $\lambda_{s,i} = 810$ nm emerges at an angle of

4. IMPLEMENTATION OF SOURCES OF 2-DIMENSIONAL ENTANGLED PHOTON STATES

approximately 3° from the axis of propagation of the pump beam. This non-collinear configuration separates the photon pairs from the residual pump beam. The polarization-entangled photon pairs (o and e -polarized photons are indistinguishable in each arm) pass through $\lambda/2$ waveplates and a CC to remove the spatial and transverse walk-off before they are coupled into single mode fibers (SMF). The spatial modes of the photon pairs, defined by SMF, are matched to the pump mode to optimize the collection of the photon pairs. A pair of 810 nm interference filters (IF), transmission bandwidth of 3 nm (Semrock, 99% transmission at 810 nm) is placed to suppress the scattered light or fluorescence generated from the BBO crystal. A pair of polarization controllers (PC) is used to ensure that the polarization of the collected photons at the output fiber is the same as the input in one arm and the polarization of the photons in the other arm is orthogonally rotated using the PC. The free phase δ between the two paths in the polarization state Eq. 3.4 is adjusted to $\delta = 0$ by tilting the CC to arrive at a state $|\phi^+\rangle$

$$|\phi\rangle_p^+ = \frac{1}{\sqrt{2}} (|H\rangle_1|H\rangle_2 + |V\rangle_1|V\rangle_2). \quad (4.3)$$

4.3.1 Polarization Correlation

The polarization analysis in each arm is performed using a combination of a $\lambda/2$ waveplate on a motorized rotation mount and a polarizing beam splitter (PBS). This allows projections onto any arbitrary linear polarization. The signals from the APDs are sent to a coincidence unit for coincidence counting.

The polarization entanglement of photon pairs prepared in this setup is tested by probing the polarization correlations in the horizontal (90°)/vertical (0°) polarization basis also known as the H/V basis (the natural basis of the type-II down-conversion process) and in a complementary basis. For the complementary basis it is common to take measurements in the $+45^\circ/-45^\circ$ basis. We quote those correlation measurements as visibilities V_{HV} and $V_{\pm 45^\circ}$, whereby the measurements are performed by rotating the $\lambda/2$ waveplates at angle α_0 and α_1 which correspond to $+45^\circ/-45^\circ$ and H/V bases, respectively. The visibility in the H/V basis is expected to

4.3 Polarization-Entangled Photons

be high since the polarization of down-conversion photon pairs generated are H and V polarized. A high visibility measurement in the $+45/-45^\circ$ basis verifies the indistinguishability of the two paths, which leads to a better quality polarization-entangled source. We observed visibilities of $V_{HV} = 99.4 \pm 1.2\%$ and $V_{45^\circ} = 99.4 \pm 1.1\%$ respectively (Fig 4.4)*.

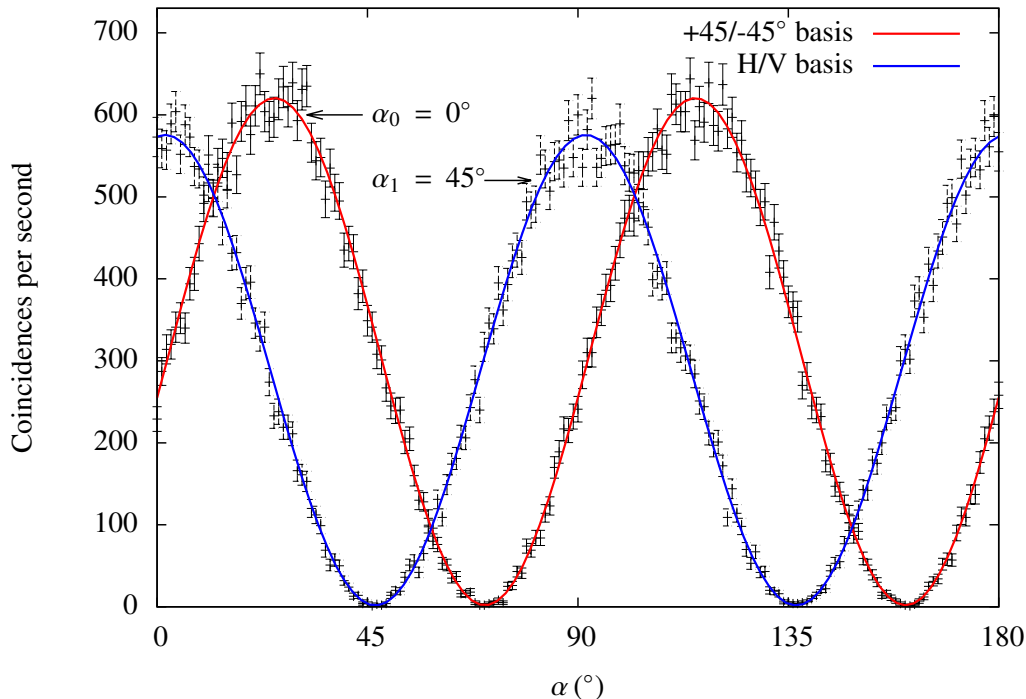


Figure 4.4: Polarization correlations measured in the H/V and $+45/-45^\circ$ basis. The observed visibilities are $V_{HV} = 99.4 \pm 1.2\%$ and $V_{45^\circ} = 99.4 \pm 1.1\%$ for the H/V and $+45/-45^\circ$ bases, respectively.

We thus ensure that our source of polarization-entangled photon pairs are of a high quality. There is no mechanical stability issues and the setup design is compact which are reasons why this configuration is often adopted in research laboratories. The practical limitation is the optical losses and polarization mode dispersion in the fiber. The optical losses inside the 810 nm single mode fiber is approximately 50% per kilometer. Polarization mode dispersion is a phenomenon where there is a slight difference in the propagation time of light with different polarization states inside the fiber.

*Refer to Section 3.2.2 for details on the measurement procedure for V_{HV} and V_{45} .

4. IMPLEMENTATION OF SOURCES OF 2-DIMENSIONAL ENTANGLED PHOTON STATES

This dispersion has a typical value of approximately a picosecond per kilometer. For the fibers we use in the experiment which are a meter long, these two factors are insignificant.

4.4 Energy-time Entangled Photons

4.4.1 Consideration of Interferometer Type

As discussed in Section 3.4, energy-time entanglement proposes several advantages compared to polarization-entanglement. This includes the possibility of implementing higher-dimensional experiments and we need not be concerned about polarization mode dispersion in the fiber. However, practical implementation is difficult due to the high sensitivity of the interferometers to mechanical instabilities and frequency instability of the pump laser. To simplify the setup, we chose to generate 2-dimensional energy-time entangled photons which requires only one unbalanced Mach-Zehnder in each arm.

We will first discuss the two possible interferometer setups, namely fiber and free-space interferometers. The most stringent condition of an interferometer is the perfect spatial mode and beam propagation overlap between the two modes. Fiber beam splitters offer the advantage of ensuring that both Gaussian modes are indistinguishable in their spatial distributions and propagation in each arm has perfect overlap. There is no active stabilization for mechanical vibrations except for temperature stabilization of the fiber. This is required since the optical path length differences changes with the room temperature. The change in refractive index inside the fiber has a typical value of $10^{-5}/\text{K}$. For a metre of fiber used in the experiment, a change in temperature of 0.1 degree Celsius causes a phase shift of more than 2π radian. However, by controlling the temperature, one can set an arbitrary phase shift in this interferometric experiment. Since the path length difference of the interferometers have to be kept to within the coherence length of the down-converted photons ($\approx 100 \mu\text{m}$), the fibers need to be cut to a certain length with a comparative accuracy.

On the other hand, the free space interferometer has less temperature

4.4 Energy-time Entangled Photons

and path length problems. The position of the mirror can be controlled using a stepper motor to reach a path length difference precision of up to $\approx 100 \mu\text{m}$. However, the difference in the beam size increases with the path length difference. This reduces the indistinguishability and results in a lower visibility. For this matter, the beam has to be collimated over a long distance, approximately 1 m in our experiment to maximize the interference visibility. In practice, this imperfection limits the possible number of interferometers and thus the maximum possible number of dimensions in the energy-time degree of freedom. In the free-space interferometer, extra work is needed to align the beam to reach high visibility. The free-space interferometer offers simpler active stabilization against mechanical vibrations. This is achieved by sending a fixed frequency reference laser beam following a path parallel to the down-converted photon pairs in the interferometer. Any vibrations on the mechanical components would be detected by this reference laser and necessary compensation for this vibration can be made. After consideration, we chose to adopt the free-space interferometer design because it is less temperature sensitive and the phase shift is easier to manipulate using an piezoelectric actuator.

For the pump laser, we used an 405 nm external cavity laser diode which shows a relatively high visibility $\geq 98\%$ in an interferometer with a path length difference of 1.5 m. A variation in the pump laser wavelength $\Delta\lambda_p$ introduces a relative phase shift of the interferometer, $\Delta\phi = 2\pi \frac{\Delta L \Delta\lambda_p}{\lambda_p^2}$, where ΔL is path length is difference. A metre in the path length difference would probably require a frequency stability of 10 MHz. A popular scheme for reducing the frequency variations down to less than 10 MHz is based on the active stabilization of a suitable stable reference frequency. However, there are few suitable atomic transition at our pump wavelength to stabilize to. Alternatively, we can shorten our data acquisition time to avoid the long term drift in the pump laser frequency.

4. IMPLEMENTATION OF SOURCES OF 2-DIMENSIONAL ENTANGLED PHOTON STATES

4.4.2 Schematic of Setup for Generation Energy-Time Entangled Photons

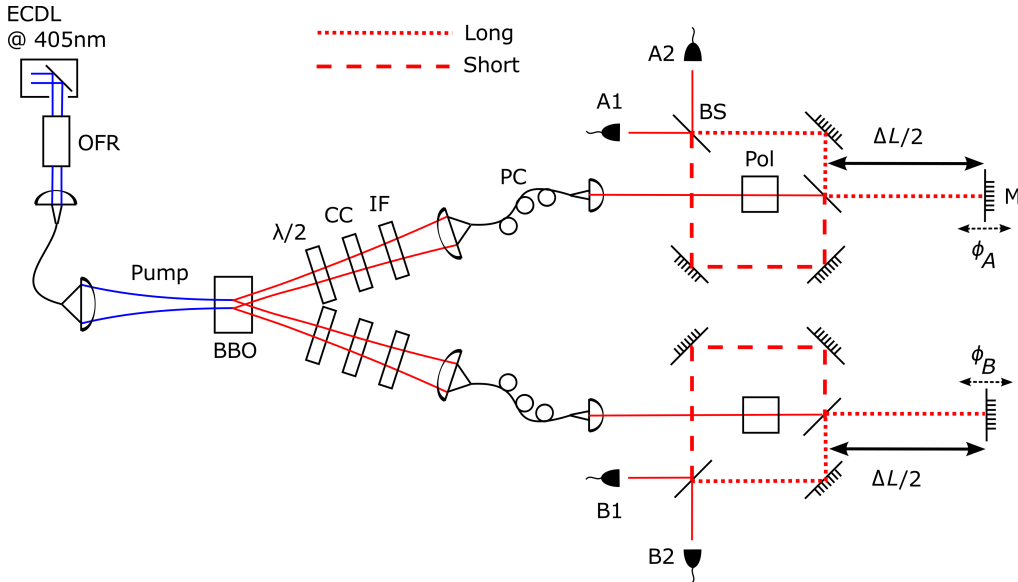


Figure 4.5: Schematic setup of a source of energy-time entangled photon pairs. The down-conversion photon pairs were sent into unbalanced Mach-Zehnder interferometers where $|0\rangle$ and $|1\rangle$ represent the short and long path, respectively. By discarding the states $|0\rangle_A|1\rangle_B$ and $|1\rangle_A|0\rangle_B$, the post-selected states $|0\rangle_A|0\rangle_B$ and $|1\rangle_A|1\rangle_B$ constitute the energy-time entangled state.

The setup for the generation of energy-time entangled photons is shown in Fig. 4.5. The condition that the delay $\Delta T = \Delta L/c$ must be smaller than the coherence time of the pump photon τ_2 is fulfilled by using the 405 nm external cavity laser diode as pump laser. This condition guarantees the coherent superposition of the photon pairs which take the short path or long path in the interferometers. Furthermore, a path length difference of $\Delta L = 0.75$ m or 2.5 ns, was chosen which can exceed our coincidence time window.

Photon pairs generated from down-conversion using a 2 mm long BBO crystal are sent into unbalanced Mach-Zehnder interferometers. For the

preliminary measurement, a pair of polarizers (Pol) are inserted in the interferometers to select one of the two states $|H\rangle_A|H\rangle_B$ and $|V\rangle_A|V\rangle_B$ generated from the down-conversion source. We introduce the long path by placing a mirror (M) at $\Delta L/2$ away from the beam splitter (BS). This long path is folded such that the retro-reflection introduces a total path length difference of $\Delta L = 0.75$ m. The Franson interference requires the mirror to be placed accurately to within the coherence length of the down-conversion photons, $l_c \approx 100 \mu\text{m}$. Therefore, the movement of the mirror is controlled by a combination of a stepper motor which moves the mirror with μm precision and a piezoelectric actuator (Thorlabs: AE0505D08F, maximum displacement of $9.1\mu\text{m}$ at 150 V) which moves the mirror with submicron precision. The voltage sent to the piezoelectric actuator changes the phase ϕ_A and ϕ_B of the interferometers. We built an external cavity laser diode which has an operating wavelength of $\lambda = 810$ nm (JDSU: 5400202, maximum output power of 50 mW) to simulate the down-conversion beam. The laser beam is visible to the naked eye and the coherence length is ≥ 1 m allowing us to align the interferometers. The two interferometers are aligned to reach an interference visibility of at least 97%.

The coincidence time window was chosen which exceeds our APD timing uncertainty. We measured the timing resolution by registering the photon pair coincidences between the two APDs. The number of coincidences is maximum when the time difference Δt between these two signals is zero. The full width at half maximum (FWHM) was measured to be approximately 1 ns (Fig. 4.6).

4.4.3 Matching the Interferometer Path Length Differences

To match the path length difference between the two interferometers, the output of one of them is directly coupled into the other interferometer input by a SMF (Fig. 4.7).

To avoid observing single photon interference effects in the interferometer itself, the coherence length of the input laser beam has to be shorter than ΔL . This warrants that the interference observed is purely due to

4. IMPLEMENTATION OF SOURCES OF 2-DIMENSIONAL ENTANGLED PHOTON STATES

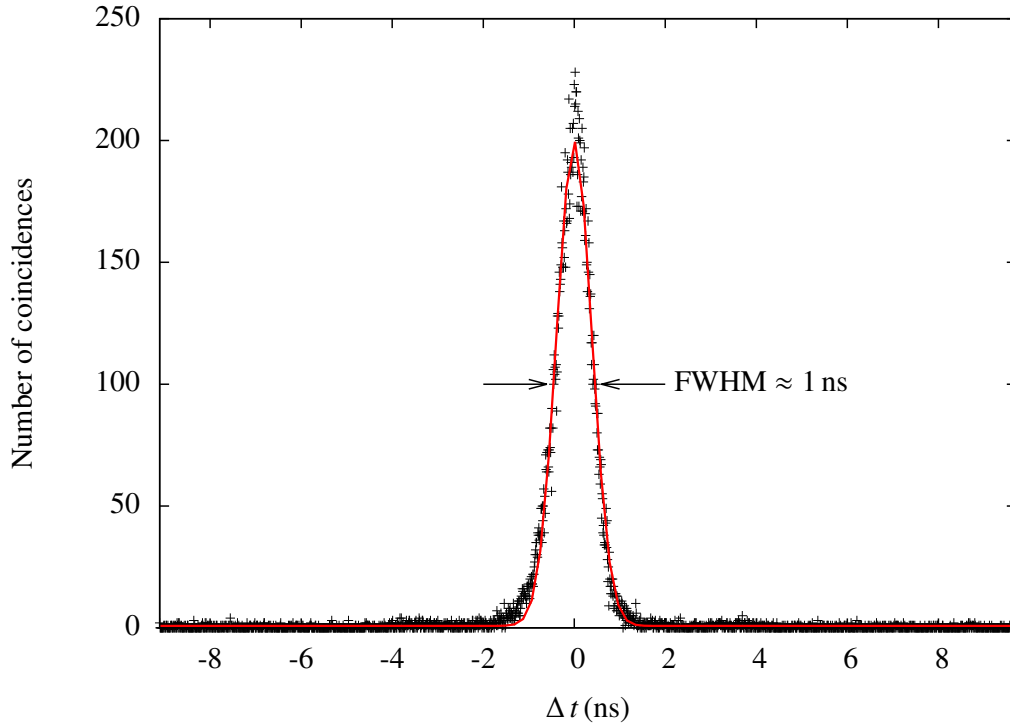


Figure 4.6: APD timing resolution. The number of coincidences is maximum when the time difference between the two signals is zero. The timing resolution is measured to be approximately 1 ns.

the path indistinguishability between the two interferometers. We chose a Ti:Sa pulsed laser which operates at 810 nm wavelength with a bandwidth of 5 nm (approximately the bandwidth of the down-conversion photons). The power is a few mW and the beam is coupled into the SMF of the input interferometer. By moving the mirror (M) using the stepper motor, once the interferometer path lengths are equalized up to the coherence length of the input beam, the two states $|0\rangle_A|1\rangle_B$ and $|0\rangle_B|1\rangle_A$ of the photons interfere (Fig. 4.8). By monitoring the signals from APD 1 or APD 2, the position of the mirror is adjusted until the maximum interference is observed. This corresponds to a matched path length difference in these two interferometers. The matching of the path lengths is verified by sending the down-converted photon pairs into both interferometers as shown in Fig. 4.5. Instead of measuring the interference between the two coupled interferometers as mentioned earlier, we measured the coincidence registered

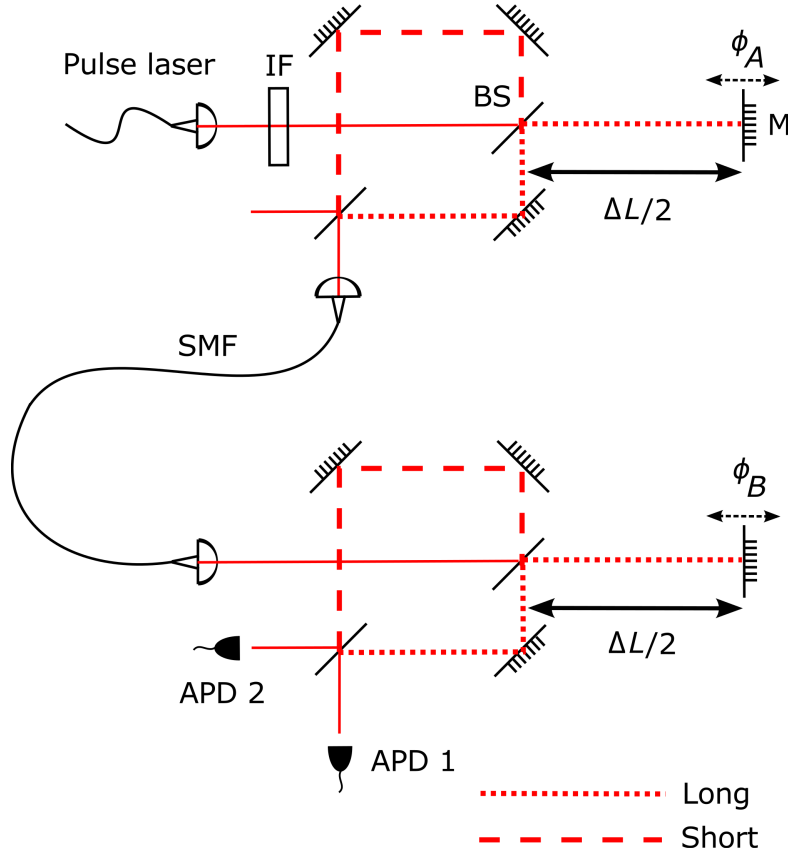


Figure 4.7: Matching the path length difference between the two interferometers. An input pulse laser was sent into the first interferometer with an interference filter (IF) at the input of the interferometer. The output is coupled into the next interferometer using a single mode fiber. By moving one of the mirrors (M) in the interferometers, once the path length difference between the two interferometers is less than the coherence length of the input beam, interference is observed and detected using APD 1 and APD 2.

between the detectors in interferometer A and B. The observed interference is a space separated interference or Franson interference. The FWHM of the envelope corresponds to the coherence length of the down-conversion photons which is approximately $l_c \approx 130 \mu\text{m}$ (Fig. 4.9). This measurement is undersampling due to the resolution of the stepper motors. In order to resolve the resolution problem and able to measure the visibility of the Franson interference, a finer scan is performed later on by using a

4. IMPLEMENTATION OF SOURCES OF 2-DIMENSIONAL ENTANGLED PHOTON STATES

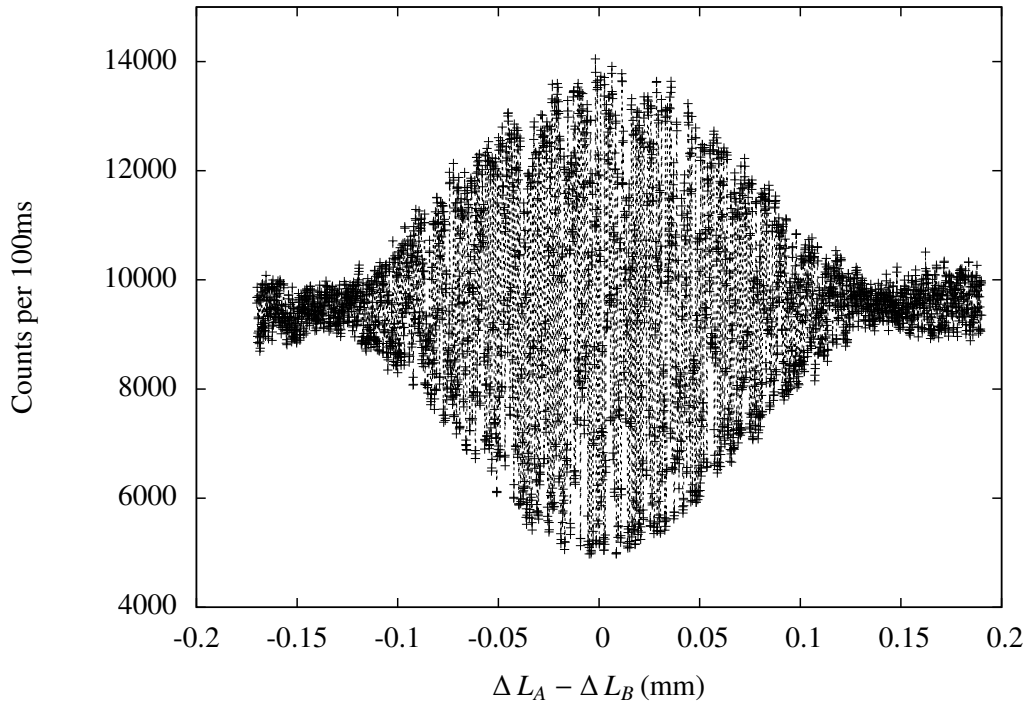


Figure 4.8: Interference (absolute photon counts) between the two states $|0\rangle_A|1\rangle_B$ and $|0\rangle_B|1\rangle_A$ showing in the APD signals (either APD 1 or APD 2). Using a pulsed laser as an input, the position of the mirror is adjusted until the observed interference is maximum. This corresponds to the two interferometer path lengths being equalized.

4.4 Energy-time Entangled Photons

piezoelectric actuator, see Section [4.4.5](#).

4. IMPLEMENTATION OF SOURCES OF 2-DIMENSIONAL ENTANGLED PHOTON STATES

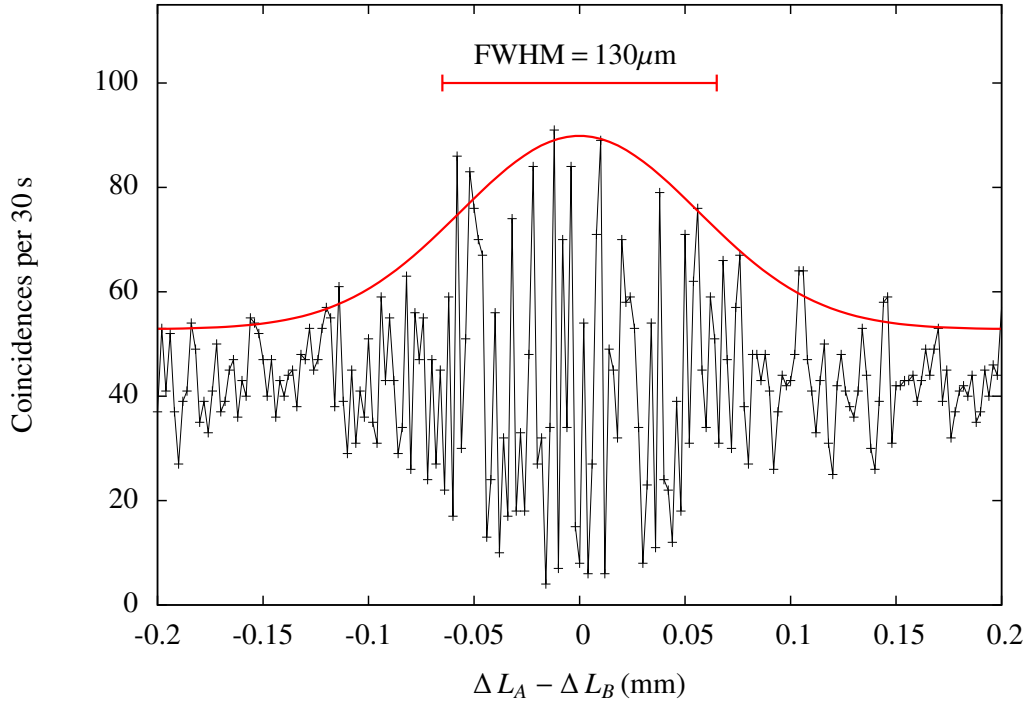


Figure 4.9: Franson interference (coincidence) between the two states $|0\rangle_A|0\rangle_B$ and $|1\rangle_B|1\rangle_A$. The coincidences are between APD A and APD B signals (A1B1, A1B2, A2B1 or A2B2, see Fig. 4.5). Using down-conversion photon pairs as an input, the Franson interference is observed while scanning the position of the mirror. The FWHM of the envelope corresponds to the coherence length of the down-converted photons which is approximately $l_c \approx 130 \mu\text{m}$. The black solid line joins the experimental data points and this measurement is undersampling due to the resolution of the scan.

4.4.4 Coincidence Time Window

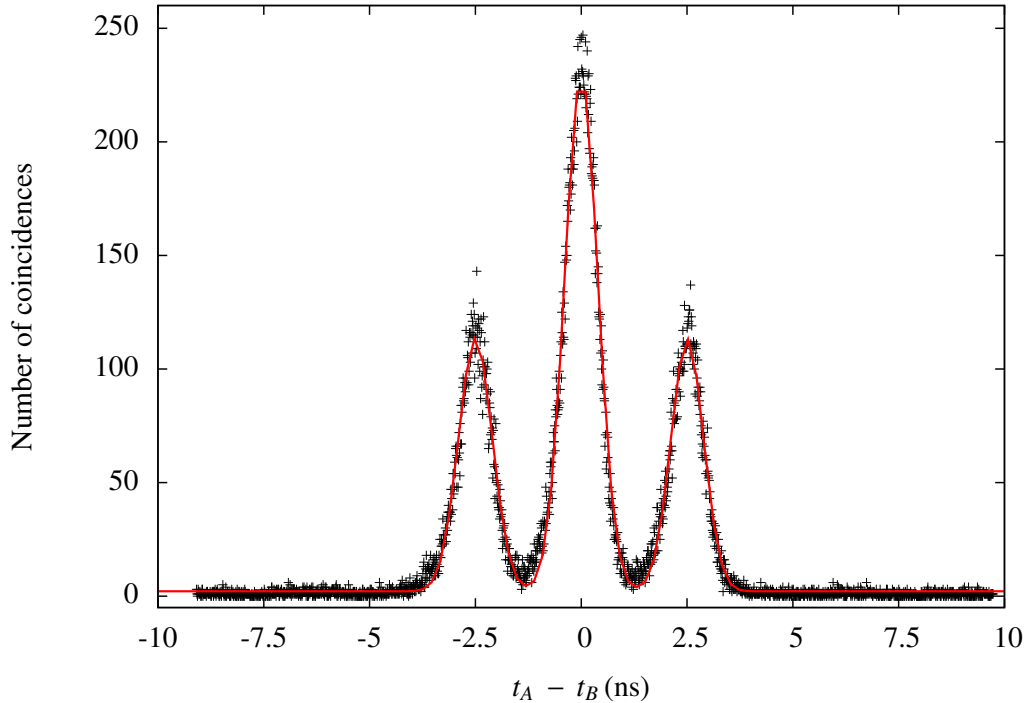


Figure 4.10: Coincidences registered between detectors in interferometer A and B without post-selection. The central peak corresponds to the indistinguishable states $|0\rangle_A|0\rangle_B$ and $|1\rangle_A|1\rangle_B$. The satellite peaks are the states $|0\rangle_A|1\rangle_B$ $|1\rangle_A|0\rangle_B$ which can be discarded by an appropriate choice of coincidence time window. The curve fit reveals the path length difference is 0.741 m or 2.47 ns and suggests that the coincidence time window should be below 2.5 ns to avoid any contribution to the coincidences from the satellite peaks.

After matching the path length differences, the subsequent procedure is to select an appropriate coincidence time window. As discussed in Section 3.3, an appropriate coincidence time window is chosen to postselect the states $|0\rangle_A|0\rangle_B$ and $|1\rangle_A|1\rangle_B$.

First, the path length difference ΔL is measured by measuring the coincidences of down-converted photon pairs between the detectors in interferometer A and B without post-selection. The coincidences are measured

4. IMPLEMENTATION OF SOURCES OF 2-DIMENSIONAL ENTANGLED PHOTON STATES

by delaying one of the detector signals, $t_A - t_B$. In Fig. 4.10, the central peak corresponds to the indistinguishable states $|0\rangle_A|0\rangle_B$ and $|1\rangle_A|1\rangle_B$. The satellite peaks are the states $|0\rangle_A|1\rangle_B$ and $|1\rangle_A|0\rangle_B$ which can be discarded by an appropriate coincidence time window. The curve fit reveals that the path length difference is 0.741 m or 2.47 ns and suggests that the coincidence time window should be below 2.5 ns to avoid any coincidences contribution from the satellite peaks. Any unwanted coincidences reduces the quality of the energy-time entangled state.

To characterize the coincidence time window of our n-channel coincidence unit [98], we measured the coincidences between two identical copies of a signal obtained from the output of an APD sent into channel 0 and 1. A variable delay t , defined as the relative delay of channel 1 with respect to channel 0, was introduced between them (Fig 4.11).

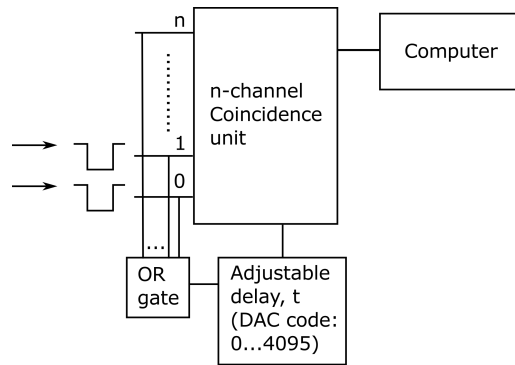


Figure 4.11: n-channel coincidence unit. The signals (photon count rates) are sent into channel 0 and 1 for coincidence counting measurement. The coincidence time window t is determined by an adjustable delay unit with a variable capacitor forming the time delay circuit. The coincidence is registered if there are two signals from different channels detected within the coincidence time window. The digital-to-analog converter (DAC) converts a digital code (0...4095) to an analog signal which controls the coincidence time window in the coincidence unit. The coincidence unit is connected to a computer for data processing. The signals from the n-channels with different arrival times are fed into an OR gate and the coincidence unit only triggers on the earliest signal among those channels.

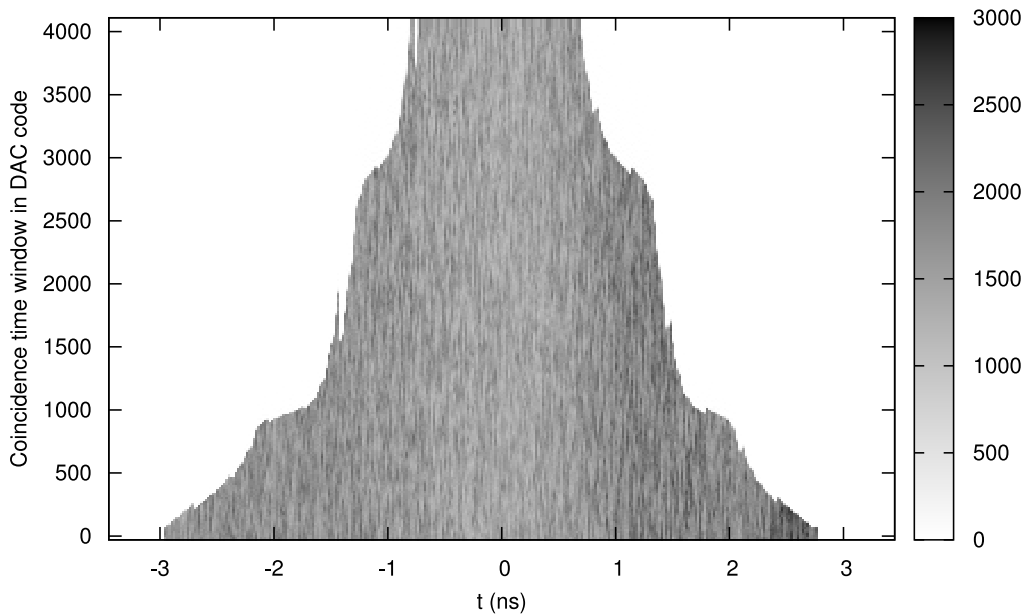


Figure 4.12: Coincidence time window (DAC code) versus time delay t , defined as relative delay of channel 1 with respect to channel 0. The right bar shows the number of coincidence events. The coincidences are maximum when the time delay between the signals are centered around zero. This graph provides us with a map between DAC code needed to set the desired coincidence time window.

This measurement was repeated by varying the coincidence time window of our coincidence unit. A 3D plot with the parameters: time window, delay, and coincidence events is plotted to obtain the coincidence time window setting (Fig. 4.12). The coincidence time window of our unit ranges from 1.6 ns to 5.6 ns. We decide to set the coincidence time window to be 1.6 ns, the smallest time window, in order to discard the unwanted coincidences contributed from the satellite peaks and postselect only the indistinguishable states $|0\rangle_A|0\rangle_B$ and $|1\rangle_A|1\rangle_B$.

4. IMPLEMENTATION OF SOURCES OF 2-DIMENSIONAL ENTANGLED PHOTON STATES

4.4.5 Energy-time Correlation

Having matched the path length difference of both interferometers and set the appropriate coincidence time window of the coincidence unit, the coincidences registered can be described as a coherent superposition of the states $|0\rangle_A|0\rangle_B$ and $|1\rangle_A|1\rangle_B$. Only when the coherence length of the pump laser is larger than ΔL then the energy-time entangled state is written as

$$|\phi\rangle_t = \frac{1}{\sqrt{2}} (|0\rangle_A|0\rangle_B - e^{i(\phi_A+\phi_B)}|1\rangle_A|1\rangle_B). \quad (4.4)$$

The laser condition must hold over the whole measurement time taken. The laser frequency instability changes the relative phase in the interferometer A and B [99]. This was monitored on the additional interferometer with the pump laser as an input. Due to the instability of the pump laser diode, the external cavity length has to be adjusted (this can be done by moving the grating with a piezoelectric actuator, which effectively changes the cavity length) to obtain an output beam with sufficiently long coherence length. A stable and high visibility interference was observed at this additional interferometer with a path length difference of approximately 1.5 m, which satisfies the condition that the coherence length of the pump photon is greater than the path length difference in the interferometers $\tau_2 > \Delta T$. We measured the visibility of the energy-time entangled state or Franson interference by changing the phase ϕ_A and ϕ_B in the interferometers. This measurement is similar to the procedure described in Section 4.4.3, but here we control the relative phases or path length differences by piezoelectric actuators. This allows a finer resolution in measuring the constructive and destructive interference of the coincidences. With a coincidence time window of 1.6 ns, by analyzing the long-short path for $|H\rangle$ photons, we observed visibilities of $V_{A1B1} = 94.3 \pm 5.2\%$ and $V_{A1B2} = 96.1 \pm 3.3\%$ for coincidences between A1B1 and A1B2, respectively (Fig 4.13). For the long-short path for $|V\rangle$ photons, we observed visibilities of $V_{A1B1} = 101.0 \pm 6.9\%$ and $V_{A1B2} = 96.6 \pm 3.3\%$ for coincidences between A1B1 and A1B2, respectively. The visibilities and their uncertainties are obtained from least-square fit of sine wave to the experimental data. The relative phase shift between the interferometer is controlled by feeding an applied voltage into the piezoelectric actuator. The stability of the inter-

4.4 Energy-time Entangled Photons

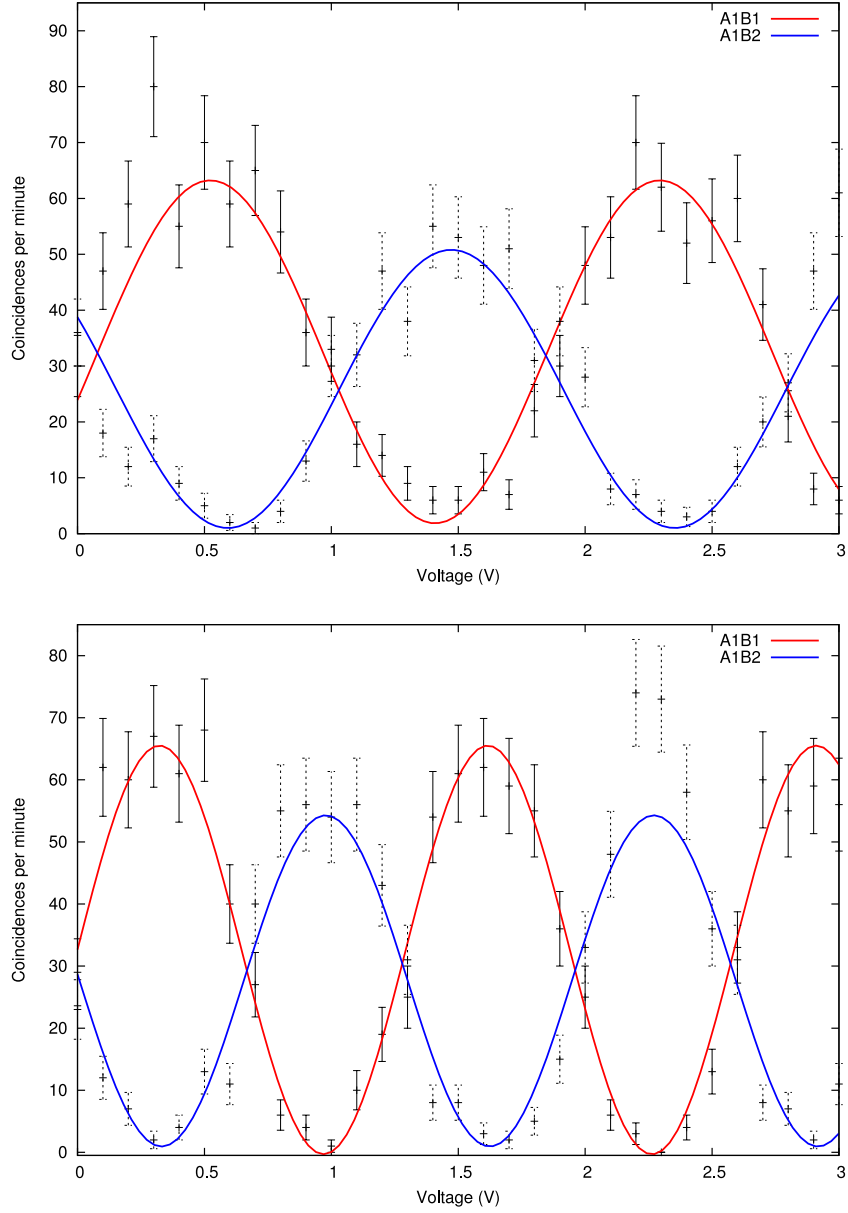


Figure 4.13: Energy-time correlation or Franson interference of long-short path for $|H\rangle$ (top) and $|V\rangle$ (bottom). The relative phase shift between the interferometers A and B is controlled by a piezoelectric actuator. (top) The observed visibilities are $V_{A1B1} = 94.3 \pm 5.2\%$ and $V_{A1B2} = 96.1 \pm 3.6\%$ for coincidences between A1B1 and A1B2, respectively. (bottom) The observed visibilities are $V_{A1B1} = 101.0 \pm 5.9\%$ and $V_{A1B2} = 96.6 \pm 3.3\%$ for coincidences between A1B1 and A1B2, respectively. The unequal periods of the visibility trace for the two interferometers is mainly due to interferometer A and B having different piezoelectric actuators.

4. IMPLEMENTATION OF SOURCES OF 2-DIMENSIONAL ENTANGLED PHOTON STATES

ferometers limits our integration time and hence results in a larger error bar in the measurement.

4.5 Summary

In the polarization-entangled source, the down-converted photon pairs generated from the BBO crystal is in a superposition state and the collection optics are positioned such that these indistinguishable photon pairs are collected efficiently. The measurement settings for the polarization basis are determined by the orientation of the waveplates in the analyzers which can be calibrated in advanced. This entangled state is well defined which facilitates further analysis this source.

This is different for the energy-time entangled source, whereby the indistinguishability between the two decay paths for photon pairs relies on the stability of the interferometers built in this experiment. Any stability issues result in the entangled state being not perfectly well-defined and the subsequent visibility measurements and analysis become less straight forward. Moreover, the measurement settings on the relative phases are not easily determined and controlled since the phases are subject to the relative stability between the two interferometers and the frequency stability of the pump laser. The solutions to this problem will be discussed in Chapter 5.

4. IMPLEMENTATION OF SOURCES OF 2-DIMENSIONAL ENTANGLED PHOTON STATES

Chapter 5

Violation of the 4-Dimensional CGLMP Inequality

In this Chapter we give a detailed overview of the implementation of a 4-dimensional entangled state and highlight the findings from our attempt to violate the 4-dimensional CGLMP inequality.

5.1 Background

In view of high-dimensional entanglement having promising applications in quantum information science, much progress has been made on the generation of high-dimensional entangled states [71, 77]. These experiments show non-classical correlations but practical applications are only conceivable when it is possible to detect these high-dimensional entangled states. Experiments reported recently in [100, 101] show that a classical d dimensional system can violate a quantum $d - 1$ dimensional system, up to $d = 4$ using the orbital angular momentum degree of freedom. However, the weakness of the witnesses defined in their experiments is that they are unable to rule out the possibility of having a classical d -dimensional state instead of a d -dimensional entangled state. The CGMLP inequality or dimension witness defined in our experiment has the advantage in identifying the classical correlations for any d -dimensional systems. Therefore we are only probing the lower bound of the d -dimensional entangled states in our experiment.

5.2 Implementation of 4-Dimensional Entangled Photons

The probing of dimensionality in this experiment was proposed by Cai [102]. The 4-dimensional entangled photons consists of a combination of a polarization and energy-time entangled photons and the state is written as,

$$|\Phi\rangle = |\phi_{\text{polarization}}^+\rangle \otimes |\phi_{\text{energy-time}}^+\rangle. \quad (5.1)$$

The above state can be further rewritten as the 4-dimensional maximally entangled state in Eq. 2.10.

The setup for the energy-time entangled experiment is modified with two interferometers in each arm to analyze the horizontal (H) and vertical (V) polarization of the entangled photons.

In Fig. 5.1, one of the polarized-entangled photon pairs was sent to Alice's side, with a polarizing beam splitter (PBS) which transmits the $|H\rangle$ photons and reflects the $|V\rangle$ photons before the photons are sent respectively into the unbalanced Mach-Zehnder interferometer. There are two separate unbalanced Mach-Zehnder interferometers, one for each polarization. After the first beam splitter (BS), the $|H\rangle$ photons which take the long path or $|V\rangle$ photons which take the short path is sent through a $\lambda/2$ waveplate which transforms $|H\rangle \rightarrow \frac{1}{\sqrt{2}}(|H\rangle + |V\rangle)$ and $|V\rangle \rightarrow \frac{1}{\sqrt{2}}(-|H\rangle + |V\rangle)$. The $|H\rangle$ photons which take the short path or $|V\rangle$ photons which take the long path is sent through a $\lambda/4$ waveplate which transforms $|H\rangle \rightarrow \frac{1}{\sqrt{2}}(|H\rangle + i|V\rangle)$ and $|V\rangle \rightarrow \frac{1}{\sqrt{2}}(i|H\rangle + |V\rangle)$. Following this, the photons recombine at the second BS which completes the Mach-Zehnder interferometer. Following each output of the second beam splitter, a PBS is placed. Photons from the output ports of the PBS were then detected with APDs. There are total of four detectors on each side corresponding to four outcomes in this measurement. For Bob's side, the setup is entirely the same except the $|H\rangle$ photons which take the short path or $|V\rangle$ photons which take the long path is sent through a $\lambda/4$ waveplate which transforms $|H\rangle \rightarrow \frac{1}{\sqrt{2}}(|H\rangle - i|V\rangle)$ and $|V\rangle \rightarrow \frac{1}{\sqrt{2}}(-i|H\rangle + |V\rangle)$. The purpose of these waveplate orientations and the phases $\phi_{P,H,V}$ are meant for the CGLMP measurement which will be discussed in the later part of this chapter.

5.2 Implementation of 4-Dimensional Entangled Photons

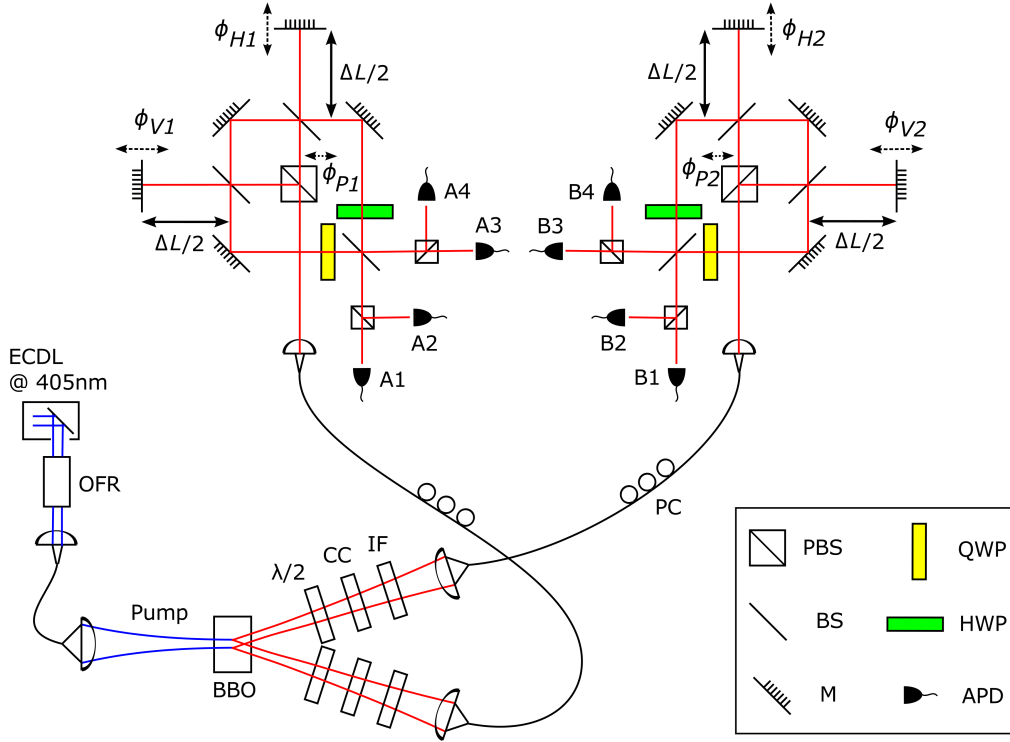


Figure 5.1: Implementation of 4-dimensional entangled photons. The scheme of energy-time entangled experiment is modified with two interferometers in each arm to analyze the horizontal and vertical polarization of the polarized-entangled photons.

There are two major disadvantages with this setup. For the CGLMP measurement, we measure $4 \times 4 = 16$ combinations of two-fold coincidences. The schematic design of the energy-time experiment introduces an inherent 50% losses for the single photon counting. The two-fold coincidence between Alice and Bob is expected to be only $0.50 \times 0.50 = 0.25$ of the total coincidences generated from down-conversion. Furthermore, the stability of the interferometers is subjected to temperature change and vibrations from the environment. The thermal expansion of aluminium optomechanics on which the optics are mounted are on the order of $\mu\text{m}/\text{K}$ which means in general there is a long term drift in the relative phase between the interferometers. In order to minimize the temperature fluctuations and vibrations from air currents, thus increasing the interferometric

5. VIOLATION OF THE 4-DIMENSIONAL CGLMP INEQUALITY

stability, the setup is enclosed in a box .

5.2.1 Optimizing the Quality of the Interferometers

The path length difference of the short path for $|H\rangle$ and $|V\rangle$ photons has to be kept within the coherence length of the down-converted photons. We applied the same technique as discussed earlier in Section 4.4.3, we equalized these two short paths using a pulsed laser as an input. A maximum visibility of the interference corresponds to the path length difference being within the coherence length of the input beam. We observed a visibility of at least 97% for this short-short path interference.

After matching the short-short path length difference, we proceed to match the path length difference of the long-short interferometers of A and B. The conditions below need to be satisfied,

$$l_H^A - s_H^A = l_V^A - s_V^A = l_H^B - s_H^B = l_V^B - s_V^B. \quad (5.2)$$

where l indicates the long path, s the short path, H for horizontal polarization, V for vertical polarization, A for Alice and B for Bob. The above condition must hold at least within the coherence length of the down-converted photons. This was accomplished in three steps similar to Section 4.4.3 but in a different order. First, we matched the long-short path length for $|H\rangle$ in Alice and Bob, then we matched the long-short path length for $|H\rangle$ in Alice and $|V\rangle$ in Bob, and lastly we matched the long-short path length for $|V\rangle$ in Alice and Bob.

The alignment of these three interferometers in one arm requires a substantial amount of work since the alignment procedure needs to be done in sequence and the corresponding mirrors need to be readjusted until the visibilities reach maximum and the path length differences need to be re-matched. The long-short path length difference is still kept to $\Delta L = 0.75$ m and the short path is kept to approximately 0.38 m which is almost the shortest path we could work with. This is because the length of the short path is determined mostly by the size of our optomechanical and optical components. We measured the visibilities for each interferometer using the pulsed laser and external cavity diode laser (ECDL). The table below summarizes the visibility measurements.

5.2 Implementation of 4-Dimensional Entangled Photons

Table 5.1: Visibility of Interferometers.

Laser input		short-short	long-short $ H\rangle$ path	long-short $ V\rangle$ path	long-long
Pulse laser, $l_c \approx 0.1$ mm	Alice	97.9%	-	-	93.0%
	Bob	98.7%	-	-	94.5%
ECDL, $l_c \geq 1$ m	Alice	98.5%	97.2%	97.2%	96.2%
	Bob	98.8%	96.8%	96.2%	95.9%

We attribute the reduction in visibility for the long-short path to the imperfect overlapping between the two spatial modes. In practice, we can maximize the first three visibilities in Table 5.1 by adjusting the path length difference and the corresponding mirrors. The difficulty of these alignments is that these interferometers share common paths and the mirrors have to be adjusted to make sure all these visibilities reach optimum. The long-long path interference suffers from a lower visibility because all the mirrors have been optimized for maximum visibility for the first three visibility measurements in Table 5.1, and hence there are no extra degrees of freedom to increase the long-long path interference visibility. It is not known why the measured visibilities in long-long path interference using the pulsed laser as input are lower than the ECDL.

5.2.2 Phase Shift Compensation

The next issue is we faced was the imperfect splitting ratio and change in polarization of the output beam from the BS. The splitting ratio is not 50:50 but instead, an unbalanced ratio of 45:55, subject to the polarization of the input light. This leads to unbalanced detector measurements and a skew in the photon counting statistics. We resolve this problem by adjusting the detector coupling in order to obtain a balanced measurement. However, the issues of unequal splitting ratio raise the concern of the accuracy in our measurement basis which cannot be solved exactly by just adjusting the detector coupling.

The second problem of the BS is that it does not maintain the polar-

5. VIOLATION OF THE 4-DIMENSIONAL CGLMP INEQUALITY

ization of the light passing through it. The observation of the short-short path interference projected on the $|H\rangle$ and $|V\rangle$ basis is not consistent with theoretical prediction. We consider mode propagation in the short-short path with the mode entering the PBS written as (Fig. 5.1)

$$a \xrightarrow{\text{PBS}} \frac{1}{\sqrt{2}}(c_H - ie^{i\phi_P} d_V) \quad (5.3)$$

$$c_H \xrightarrow{\text{QWP}} \frac{1}{\sqrt{2}}(c_H \pm ic_V) \quad (5.4)$$

$$d_V \xrightarrow{\text{HWP}} \frac{1}{\sqrt{2}}(-d_H + d_V) \quad (5.5)$$

where the plus sign indicates the setting for Alice and minus sign for Bob. The four modes for Alice and Bob after the BS are

$$\begin{pmatrix} \text{A1} \\ \text{A2} \\ \text{A3} \\ \text{A4} \end{pmatrix} = \frac{1}{2\sqrt{2}} \begin{pmatrix} i + ie^{i\phi_P} \\ -i - e^{i\phi_P} \\ 1 - e^{i\phi_P} \\ 1 + ie^{i\phi_P} \end{pmatrix}, \quad (5.6)$$

$$\begin{pmatrix} \text{B1} \\ \text{B2} \\ \text{B3} \\ \text{B4} \end{pmatrix} = \frac{1}{2\sqrt{2}} \begin{pmatrix} i + ie^{i\phi_P} \\ i - e^{i\phi_P} \\ 1 - e^{i\phi_P} \\ -1 + ie^{i\phi_P} \end{pmatrix}. \quad (5.7)$$

The probabilities of detecting these modes are

$$\begin{pmatrix} |\text{A1}|^2 \\ |\text{A2}|^2 \\ |\text{A3}|^2 \\ |\text{A4}|^2 \end{pmatrix} = \frac{1}{4} \begin{pmatrix} 1 + \cos \phi_P \\ 1 + \sin \phi_P \\ 1 - \cos \phi_P \\ 1 - \sin \phi_P \end{pmatrix}, \quad (5.8)$$

$$\begin{pmatrix} |\text{B1}|^2 \\ |\text{B2}|^2 \\ |\text{B3}|^2 \\ |\text{B4}|^2 \end{pmatrix} = \frac{1}{4} \begin{pmatrix} 1 + \cos \phi_P \\ 1 - \sin \phi_P \\ 1 - \cos \phi_P \\ 1 + \sin \phi_P \end{pmatrix}. \quad (5.9)$$

By measuring these interferences in the $|H\rangle$ and $|V\rangle$ basis, the phase shift values obtained do not agree to each other with a discrepancy of at least half a radian (Fig. 5.2). This is mainly because the BS introduces an anomalous phase shift between the $|H\rangle$ and $|V\rangle$ components, which effectively changes the polarization. To recover the polarization after the beam passes through the BS, a quartz plate is placed before the BS input. The quartz plates correct the relative phases of the $|H\rangle$ and $|V\rangle$ components, hence maintaining the original input polarization.

5.2 Implementation of 4-Dimensional Entangled Photons

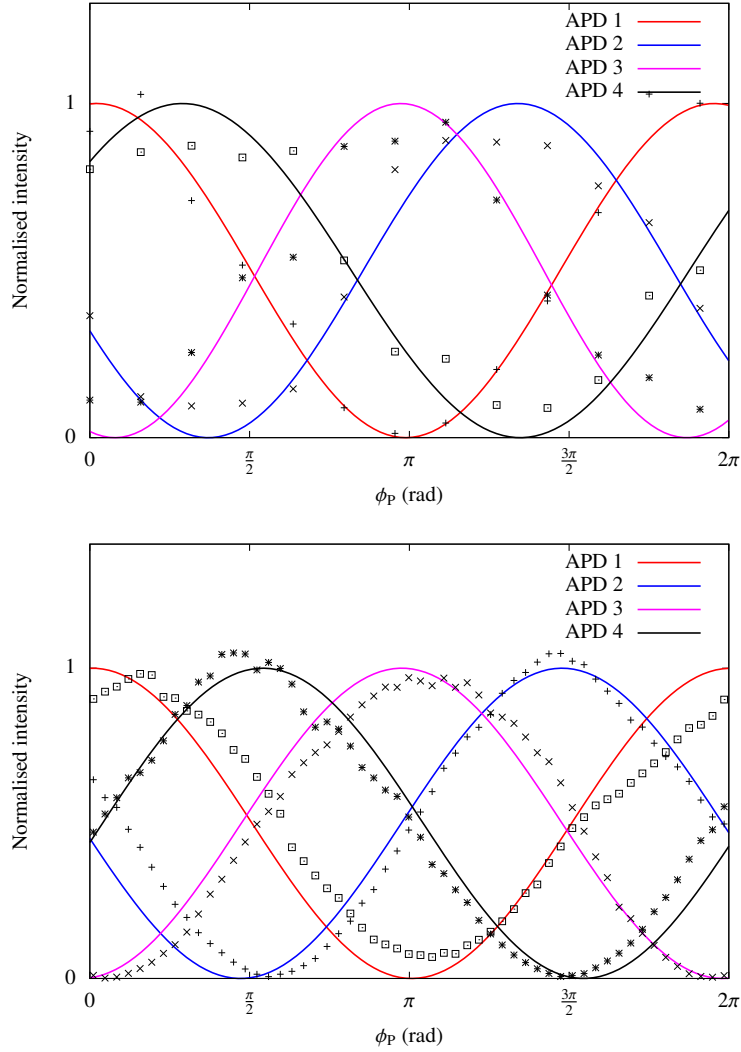


Figure 5.2: Compensation of the phase shift by the quartz plate. (top) The interference of the short-short path as measured by four APDs without quartz plate. A phase shift introduced by the beam splitter (BS) was observed between APD 1 and 3 (projected on $|H\rangle$ basis) and APD 2 and 4 (projected on $|V\rangle$ basis). The phase shift is compensated by introducing two quartz plates with each placed before the BS input. (bottom) The observed interference is in agreement with the theoretical prediction (Eq. 5.9) after compensating for the anomalous phase shift due to the beam splitter (BS) with quartz plates.

5. VIOLATION OF THE 4-DIMENSIONAL CGLMP INEQUALITY

5.2.3 Quality of the 4-dimensional Entangled State

We measured the visibility of this source separately, namely the visibility of the polarization correlation, energy-time correlation for $|H\rangle$, and energy-time correlation for $|V\rangle$. These visibility measurements have been mentioned in the previous sections and we summarized the result in Table 5.2.

Table 5.2: Visibility of different entangled source.

Type of entangled source	Visibility
Polarization	$\geq 99.4\%$
Energy-time, $ H\rangle$	$\geq 94.3\%$
Energy-time, $ V\rangle$	$\geq 96.6\%$

The total coincidences or sum of all 16 possible 2-fold coincidences is 930 coincidences per minute. The main objective of this experiment is not to develop a high brightness entangled source and we did not put much effort in increasing the total number of coincidences. The main losses came from the interferometer design and the coupling from the source to the detectors.

5.2.4 Piezoelectric Actuator

The piezoelectric actuator transforms electrical energy into precisely controlled mechanical displacements. They are ideal for applications requiring rapid, precise positional changes on the nanometer or micrometer scale. However the non-linearity of the mechanical displacements or hysteresis is a problem since the displacement varies with the direction of the applied voltage. This affects the accuracy of our phase measurements in the interferometers. The hysteresis effect was characterized using our existing interferometric setup. Our measurement shows that hysteresis is present even though the applied voltage is 20 V, which does not exceed the maximum applied voltage of 150 V.

Using the JDSU laser diode as an input laser, we measured the single photon interference signal generated from the interferometer by increasing

5.2 Implementation of 4-Dimensional Entangled Photons

and decreasing the applied voltage to the piezoelectric actuator. The values of the phases are extracted to study the displacement behaviour of the piezoelectric actuator. The hysteresis curve of displacement versus voltage is mapped out for different voltage step sizes, namely 0.05 V, 0.5 V, and 1 V. Fig. 5.3 shows that the displacement takes different paths depending on the direction of the applied voltage and the voltage step size. These different step sizes contribute to the phase setting error ranging from approximately 0.4rad to 0.6rad. Since the hysteresis curve is always reproducible, it suggests that consistent displacement can always be reproduced using the same voltage if the voltage is always reset to origin.

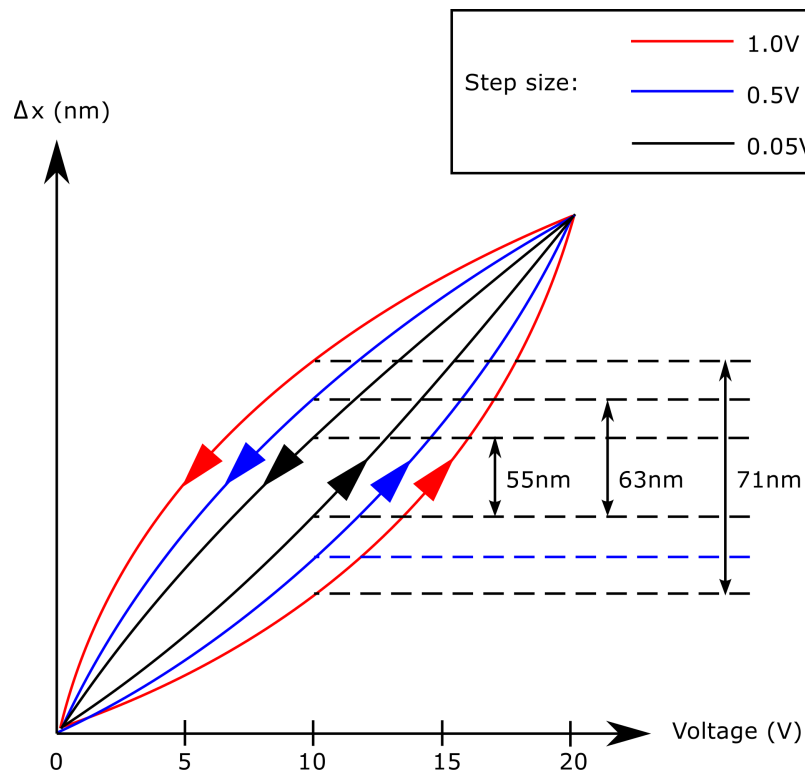


Figure 5.3: Hysteresis curve with displacement versus voltage mapped out for different voltage step sizes, namely 0.05 V, 0.5 V, and 1 V. The displacement deviation varies from 0.4 rad to 0.6 rad depending on the step size. The displacement deviation was calculated at 10 V, a median value of the applied voltage in the experiment. The hysteresis curve is a conceptual drawing and may not be to scale.

5. VIOLATION OF THE 4-DIMENSIONAL CGLMP INEQUALITY

However, it is discovered that applying the voltage in one direction does not necessarily reproduce the original displacement even though the voltage is reset to origin. With an input voltage of 20 V in steps of 1 V, there is still a consistent error of at least 0.5 rad in reproducing the phase measurement values. This error slowly reduces to approximately 0.02 rad after the step size is decreased to 0.05 V. Assuming the interferometric setup is stable for this duration of time, the relative phases in the interferometers can be measured and set accordingly.

5.2.5 Stabilizing the Interferometers

The stabilization scheme requires the ability of the piezoelectric actuator to reproduce the relative phase settings in the interferometers. In this experiment, a beam from an external cavity laser diode is used to simulate the down-converted photons in order to measure the relative phases in the interferometers. In order to measure the short-short path interference, shutters are installed to block the long path for $|H\rangle$ and $|V\rangle$ photons. For measuring the long-short path interference for $|H\rangle$ ($|V\rangle$) photons, the long path for $|V\rangle$ ($|H\rangle$) photons is blocked by the shutters. By scanning the piezoelectric actuators, these three individual interference signals are measured separately which allow us to extract the phases by fitting the visibility curves. Once the relation between the phase and voltage is extracted, we can implement the stabilization scheme by setting the required phases to the required values. For this reason the piezoelectric actuator is studied in detail in Section 5.2.4 to ensure that the phases are measured and set correctly. To verify that our stabilization scheme works accordingly, we measured the output of the interferometer by setting the relative phase beginning from 0 to 2π . The measurement was repeated several times to verify that these measurement were reproducible in order to assess the uncertainty of our phase settings. In Fig. 5.4, the step size of the input phases is 0.5 rad and the plot is the best fit curve for each measurement. We estimate the uncertainty of the set phases to be 0.1 rad.

In our experiment, the piezoelectric actuators play two major roles. We used them to stabilize the interferometers and set the required phase settings in the measurements. The alternative approach is to send a reference

5.2 Implementation of 4-Dimensional Entangled Photons

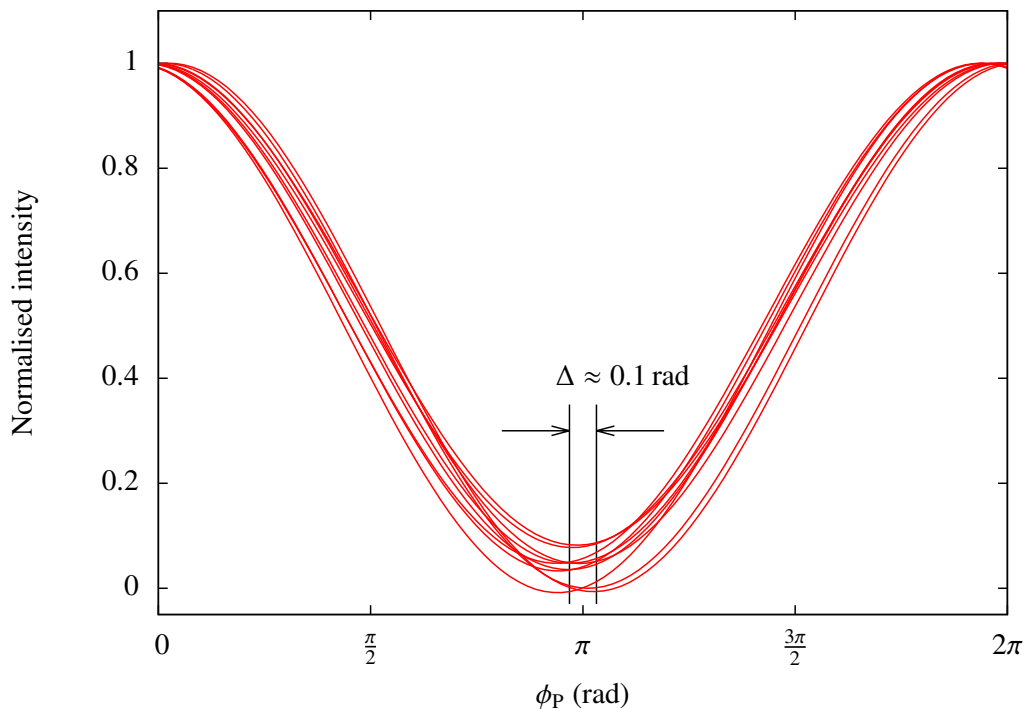


Figure 5.4: The uncertainty of the phase setting is approximately 0.1 rad.

laser beam into the interferometer. The interferometer is then locked to the error signals generated from the outputs of interferometer. The relative phases can be set by placing a very thin rotatable cover slip in the optical path length of the interferometer and the phase introduced by the cover slip can be calibrated. However, this strategy does not apply in our experiment since there are three interferometers which share common paths.

In summary, the main source of error of the phase settings comes from the long duration (5~10 minutes) taken to scan the piezoelectric actuators. This is because we run through two hysteresis cycles to make sure the set phases are accurate. The interferometers are enclosed in a box to provide better passive stability during the measurement.

As discussed in Section 4.4.5, the frequency stability of the pump laser affects the energy-time correlation. The residual pump beam after the BBO crystal is sent to a Michelson interferometer with a path length difference of 1.5 m. The interferometer is misaligned to produce a few fringes projected on the CCD camera for the purpose of locking. The high frequency drift in the observed fringes rule out the possibility of vibration

5. VIOLATION OF THE 4-DIMENSIONAL CGLMP INEQUALITY

and thermal drift of the mechanical components. The grating is controlled by attaching a piezoelectric actuator which ensures the fringes are always locked. The interferometer is enclosed in a box to minimize the instability of the interferometer. This ensures that the feedback is compensating for the frequency drift of the pump laser and not of the interferometer.

5.3 Measurement Settings

In the CGLMP paper [30] discussed the Eq. 2.5, a maximally-entangled state of a two d -dimensional system has the nondegenerate eigenvectors

$$\begin{aligned} |k\rangle_{A,a} &= \frac{1}{\sqrt{d}} \sum_{j=0}^{d-1} e^{i\frac{2\pi}{d}j(k+\alpha_a)} |j\rangle_A, \\ |l\rangle_{B,b} &= \frac{1}{\sqrt{d}} \sum_{j=0}^{d-1} e^{i\frac{2\pi}{d}j(-l+\beta_b)} |j\rangle_B, \end{aligned} \quad (5.10)$$

with operators A_a , $a = 1, 2$ measured by Alice and B_b , $b = 1, 2$ measured by Bob, and $\alpha_1 = 0$, $\alpha_2 = \frac{1}{2}$, $\beta_1 = \frac{1}{4}$ and $\beta_2 = -\frac{1}{4}$. Eq. 5.10 has been shown to maximize the violation of the CGLMP inequality for the maximally entangled state of two d -dimensional system [28, 103]. We consider a dimensionality of $d = 4$ and expand the eigenvectors

$$\begin{aligned} |k=0\rangle_{A,1} &= |0\rangle + |1\rangle + |2\rangle + |3\rangle \\ |k=1\rangle_{A,1} &= |0\rangle + i|1\rangle - |2\rangle - i|3\rangle \\ |k=2\rangle_{A,1} &= |0\rangle - |1\rangle + |2\rangle - |3\rangle \\ |k=3\rangle_{A,1} &= |0\rangle - i|1\rangle - |2\rangle + i|3\rangle \\ \\ |k=0\rangle_{A,2} &= |0\rangle + e^{i\frac{\pi}{4}}|1\rangle + e^{i\frac{\pi}{2}}|2\rangle + e^{i\frac{3\pi}{4}}|3\rangle \\ |k=1\rangle_{A,2} &= |0\rangle + ie^{i\frac{\pi}{4}}|1\rangle - e^{i\frac{\pi}{2}}|2\rangle - ie^{i\frac{3\pi}{4}}|3\rangle \\ |k=2\rangle_{A,2} &= |0\rangle - e^{i\frac{\pi}{4}}|1\rangle + e^{i\frac{\pi}{2}}|2\rangle - e^{i\frac{3\pi}{4}}|3\rangle \\ |k=3\rangle_{A,2} &= |0\rangle - ie^{i\frac{\pi}{4}}|1\rangle - e^{i\frac{\pi}{2}}|2\rangle + ie^{i\frac{3\pi}{4}}|3\rangle \end{aligned}$$

5.3 Measurement Settings

$$\begin{aligned}
|l=0\rangle_{B,1} &= |0\rangle + e^{i\frac{\pi}{8}}|1\rangle + e^{i\frac{\pi}{4}}|2\rangle + e^{i\frac{3\pi}{8}}|3\rangle \\
|l=1\rangle_{B,1} &= |0\rangle - ie^{i\frac{\pi}{8}}|1\rangle - e^{i\frac{\pi}{4}}|2\rangle + ie^{i\frac{3\pi}{8}}|3\rangle \\
|l=2\rangle_{B,1} &= |0\rangle - e^{i\frac{\pi}{8}}|1\rangle + e^{i\frac{\pi}{4}}|2\rangle - e^{i\frac{3\pi}{8}}|3\rangle \\
|l=3\rangle_{B,1} &= |0\rangle + ie^{i\frac{\pi}{8}}|1\rangle - e^{i\frac{\pi}{4}}|2\rangle - ie^{i\frac{3\pi}{8}}|3\rangle \\
\\
|l=0\rangle_{B,2} &= |0\rangle + e^{-i\frac{\pi}{8}}|1\rangle + e^{-i\frac{\pi}{4}}|2\rangle + e^{-i\frac{3\pi}{8}}|3\rangle \\
|l=1\rangle_{B,2} &= |0\rangle - ie^{-i\frac{\pi}{8}}|1\rangle - e^{-i\frac{\pi}{4}}|2\rangle + ie^{-i\frac{3\pi}{8}}|3\rangle \\
|l=2\rangle_{B,2} &= |0\rangle - e^{-i\frac{\pi}{8}}|1\rangle + e^{-i\frac{\pi}{4}}|2\rangle - e^{-i\frac{3\pi}{8}}|3\rangle \\
|l=3\rangle_{B,2} &= |0\rangle + ie^{-i\frac{\pi}{8}}|1\rangle - e^{-i\frac{\pi}{4}}|2\rangle - ie^{-i\frac{3\pi}{8}}|3\rangle \quad (5.11)
\end{aligned}$$

In order to obtain the required measurement settings in this experiment, we begin with the mode propagation (Fig. 5.5)

$$\begin{aligned}
a_{H,k} \rightarrow & -ie^{i\phi_H}(-ic_{H,k+1} - ic_{V,k+1} + d_{H,k+1} - d_{V,k+1}) \quad (5.12) \\
& + c_{H,k} \mp ic_{V,k} - id_{H,k} \pm d_{V,k},
\end{aligned}$$

$$\begin{aligned}
a_{V,k} \rightarrow & e^{i\phi_P}e^{i\phi_V}(\mp c_{H,k+1} - ic_{V,k+1} \pm id_{H,k+1} + d_{V,k+1}) \quad (5.13) \\
& + e^{i\phi_P}(-c_{H,k} + c_{V,k} - id_{H,k} - id_{V,k}),
\end{aligned}$$

with an upper sign for Alice and lower sign for Bob since the QWP waveplate setting for Alice transforms $|H\rangle \rightarrow \frac{1}{\sqrt{2}}(|H\rangle + i|V\rangle)$ and vertical polarization $|V\rangle \rightarrow \frac{1}{\sqrt{2}}(i|H\rangle + |V\rangle)$ and QWP waveplate setting for Bob transforms $|H\rangle \rightarrow \frac{1}{\sqrt{2}}(|H\rangle - i|V\rangle)$ and $|V\rangle \rightarrow \frac{1}{\sqrt{2}}(-i|H\rangle + |V\rangle)$. The subscript k represents the short path and $k+1$ represents the long path. Using Eq. 5.12 and 5.13, we expressed the modes in the first ($k=0$) and second ($k=1$) time-bin and modes in the second ($k=1$) and third ($k=2$) time-bin. We post-selected the mode in second ($k=1$) time-bin only and wrote the output port c and d as

$$\begin{aligned}
c_H &= ie^{-i\phi_H}|0\rangle \mp e^{-i\phi_P}e^{-i\phi_V}|1\rangle - e^{-i\phi_P}|2\rangle + |3\rangle, \\
d_V &= -e^{-i\phi_H}|0\rangle + e^{-i\phi_P}e^{-i\phi_V}|1\rangle + ie^{-i\phi_P}|2\rangle \pm |3\rangle, \\
d_H &= e^{-i\phi_H}|0\rangle \mp ie^{-i\phi_P}e^{-i\phi_V}|1\rangle + ie^{-i\phi_P}|2\rangle + i|3\rangle, \\
c_V &= ie^{-i\phi_H}|0\rangle + ie^{-i\phi_P}e^{-i\phi_V}|1\rangle + e^{-i\phi_P}|2\rangle \pm i|3\rangle. \quad (5.14)
\end{aligned}$$

where $|0\rangle = a_{H,0}|\text{vac}\rangle$, $|1\rangle = a_{V,0}|\text{vac}\rangle$, $|2\rangle = a_{V,1}|\text{vac}\rangle$, and $|3\rangle = a_{H,1}|\text{vac}\rangle$.

5. VIOLATION OF THE 4-DIMENSIONAL CGLMP INEQUALITY

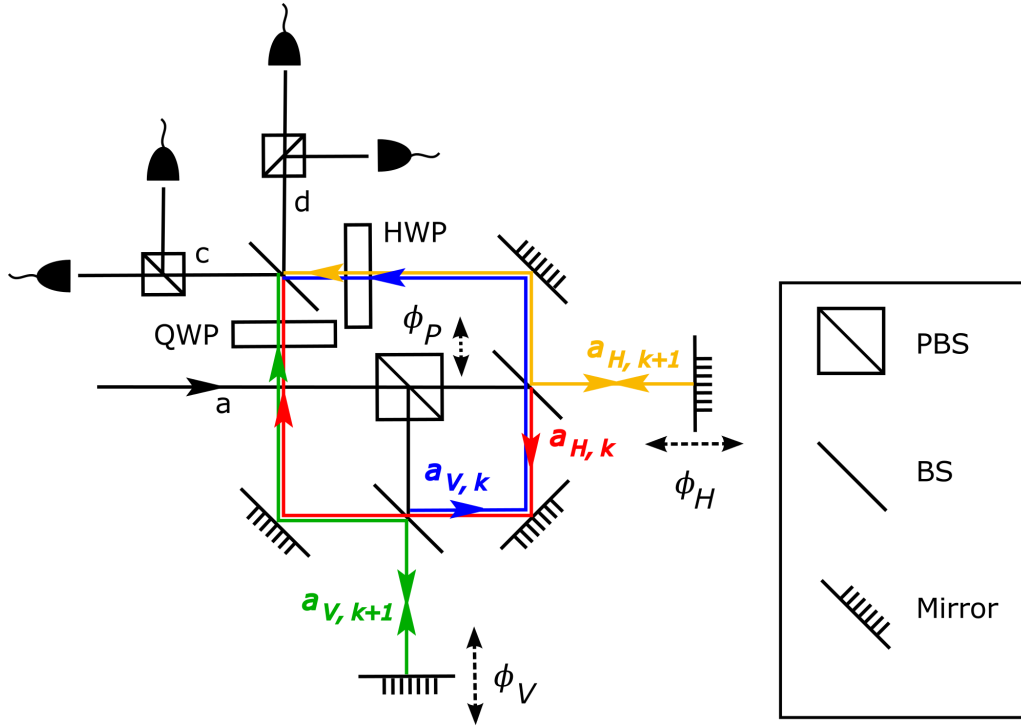


Figure 5.5: Schematic of the measurement unit on either Alice's or Bob's side. Mode a enters the PBS. The subscript k represents the short path and $k + 1$ represents the long path. The transmitted mode after the polarizing beam splitter (PBS) is split into two modes by a beam splitter (BS). The two modes are $a_{H,k}$ which passes through the QWP waveplate and $a_{H,k+1}$ which accumulates phase ϕ_H and passes through the HWP. The reflected mode after the PBS is split into two modes by a BS. The two modes are $a_{V,k}$ which passes through the HWP waveplate and $a_{V,k+1}$ which accumulates phase ϕ_V and passes through the QWP.

We compared Eq. 5.14 and Eq. 5.11 in order to extract the required ϕ_{P1} , ϕ_{P2} , ϕ_{H1} , ϕ_{H2} , ϕ_{V1} , and ϕ_{V2} phase settings. The required phase settings are extracted as shown in the Table 5.3, where A_i and B_i are the measurement settings for Alice and Bob respectively. We need to measure 2-fold coincidences between Alice and Bob by choosing the measurement settings A_0B_0 , A_0B_1 , A_1B_0 , and A_1B_1 . Refer to table 2.1, for a 2 dimensional quantum system, the maximum violation of $I_{2222} = 0.2071$ and for a

5.4 Experimental Results & Conclusions

Table 5.3: The choices of phases in the interferometers to probe the 4-dimensional entangled state for A_0 , A_1 , B_0 and B_1 settings.

	ϕ_P	ϕ_H	ϕ_V
A_0	$-\pi$	$\frac{\pi}{2}$	0
A_1	$\frac{5\pi}{4}$	$\frac{5\pi}{4}$	$\frac{\pi}{4}$
B_0	$-\frac{9\pi}{8}$	$\frac{\pi}{8}$	$\frac{7\pi}{8}$
B_1	$\frac{9\pi}{8}$	$\frac{7\pi}{8}$	$\frac{9\pi}{8}$

3 dimensional quantum system, the maximum violation of $I_{2233} = 0.30495$. In order to show that the quantum system has a dimensionality of 4, we aim to achieve a value between 0.30495 and 0.33609. Any values less than zero indicates the system is classical as discussed in Section 2.2.1.

5.4 Experimental Results & Conclusions

With a maximally entangled state $|\Phi\rangle = |\phi_{\text{polarization}}^+\rangle \otimes |\phi_{\text{energy-time}}^+\rangle$ as the input, we measured the coincidence rates for 30 seconds in each setting. However, the total time taken to perform this measurement took approximately 7 minutes. More than 6 minutes were actually used to measure and set the relative phases in the three interferometers. The applied voltages to the piezoelectric actuators had a 0.1 V step size, a reasonably slow rate. The alternative solution is to replace the piezoelectric actuator fitted with a strain gauge. The actuator under a compressive loading generates an electric charge that is directly proportional to the force applied. The feedback voltage converted from the electric charge can provide a linear operation of the piezoelectric actuator [104].

We measured the CGLMP violation to be $I_{2244} = 0.30 \pm 0.04$. This value indicates that the state of the system is in 3 dimensions since this value exceeds the maximum violation of a qubit system. Several measurement shows that the violation we measured exceeds I_{2233} , hinting that there is a possibility of the state is in 4 dimensions but this is subject to the accuracy of our measurements since the error bar is too large for us to make

5. VIOLATION OF THE 4-DIMENSIONAL CGLMP INEQUALITY

such a claim.

Our experiment is limited by the low coincidence rates and the stability of the experimental setup which results in a relatively large error in our final measurements even though the polarized and energy-time entangled photons exhibit a high visibility in their respective polarization and energy-time correlation. Since a substantial amount of time was spent locating the individual phase settings, this increased the probability of our experimental setup being affected by the stability of the interferometers and frequency of the pump laser. The frequency stability of the pump laser is currently being addressed. We remain uncertain about the tolerance of our phase settings in this CGLMP inequality measurement. Given that the upper and lower bound of this inequality is smaller than our error bar in our measurement, an increase in data acquisition time and coincidence rates may help to resolve this problem. An alternative suggestion is to use a non-maximally entangled state as an input increases the upper bound of this inequality, $I_{2244}^{\max} = 0.364762$, which means that we can afford a bigger error bar.

Chapter 6

Final Remarks

The experimental scheme to encode states in a 4-dimensional Hilbert space into entangled photon states has been presented. The hyperentanglement involving the polarization and energy-time degrees of freedom of the photons was analyzed with four outputs for each signal and idler photon pairs. A high dimensional entangled state lowers the threshold of the detection efficiency for loophole free Bell experiments [28]. In the earlier part of Chapter 4, the collection efficiency of the photon pairs generated from the BBO crystal and detector efficiency of the APD used were characterized. We showed that a loophole free experiment using type-II down-conversion using a BBO crystal is difficult to implement because the collection efficiency of the source does not exceed the minimum value required [28].

We focused on a test of the CGLMP inequality measurement. Nevertheless, the losses introduced by the interferometers lead to a large decrease in the coincidence count rate. To increase the coincidence count rates, we can utilize periodically-poled lithium niobate (PPLN) [105] or potassium titanyl phosphate (PPKTP) [106] crystals for both type-I and II down-conversion respectively. Since PPKTP possess a larger effective non-linear coefficient (typically 5 times higher than BBO crystal [107]), the observed down-conversion efficiencies using a long PPKTP crystal has been reported up to be 4 orders of magnitude higher than the BBO crystal. This is because the yield of the down-converted photons is proportional to the square of the product of the effective non-linear coefficient and the crystal length. Furthermore, the reduction of bandwidth of the down-converted photon

6. FINAL REMARKS

pairs may improve the energy-time correlation because the path length differences in the interferometers are less stringent. Lastly, the complete suppression of the spatial walk-off eliminates the need for additional compensation crystals.

The question that now remains is whether we have achieved the goal of implementing a 4-dimensional entangled source. In a limited sense the answer is yes since we observed Franson interference using our polarized-entangled photons. The remaining issues of the frequency stability of the pump laser is currently being addressed and the piezoelectric actuator fitted with strain gauge are in place and have been characterized. We believe these may help in improving the accuracy of our measurements and thus reduce the error in our measurement of the CGLMP inequality.

For a fundamental test, we have demonstrated the concept of dimensionality, which can be experimentally assessed. The measurement statistics collected reveals the relevant information about an unknown system, without referring to the internal working of the source. There are different attempts to prepare experiments in higher dimensions using various degrees of freedom. Recently, an experiment reported a 50-dimensional two-photon using orbital angular momentum entanglement [108], but the violation of Bell's inequality is difficult to implement. Nevertheless, this points to the possibility of implementing new experiments such as loophole-free Bell test experiments in the future.

Bibliography

- [1] Heisenberg, W. Über den anschaulichen Inhalt der quantentheoretischen Kinematik und Mechanik. *Z. für Phys*, **43**:172–198, 1927. [1](#), [6](#)
- [2] Benjamin Schumacher. Quantum coding. *Physical Review A*, **51**:2738–2747, 1995. [2](#)
- [3] P. W. Shor. Polynomial-Time Algorithms for Prime Factorization and Discrete Logarithms on a Quantum Computer. *SIAM Journal on Scientific and Statistical Computing*, **26**:1484, 1997. [2](#), [35](#)
- [4] Lieven M. K. Vandersypen, Matthias Steffen, Gregory Breyta, Costantino S. Yannoni, Mark H. Sherwood, and Isaac L. Chuang. Experimental realization of Shor’s quantum factoring algorithm using nuclear magnetic resonance. *Nature*, **414**:883–887, 2001. [2](#)
- [5] Lov K. Grover. Quantum Mechanics Helps in Searching for a Needle in a Haystack. *Physical Review Letters*, **79**:325–328, 1997. [2](#)
- [6] J. Ahn, T. C. Weinacht, P. H. Bucksbaum. Information Storage and Retrieval Through Quantum Phase. *Science*, **287**:463–465, 2000. [2](#)
- [7] C. H. Bennett and G. Brassard. Proceedings of the IEEE International Conference on Computers, Systems, and Signal Processing. In *Quantum Cryptography: Public key distribution and coin tossing*, pages 175–179, Bangalore, 1984. [2](#)
- [8] C. H. Bennett, F. Bessette, G. Brassard, L. Salvail, and J. Smolin. Experimental quantum cryptography. *Journal of Cryptology*, **5**:3–28, 1992. [2](#)

BIBLIOGRAPHY

- [9] Charles H. Bennett, Gilles Brassard, Claude Crpeau, Richard Jozsa, Asher Peres, and William K. Wootters. Teleporting an unknown quantum state via dual classical and Einstein-Podolsky-Rosen channels. *Physical Review Letters*, **70**:1895, 1993. [2](#)
- [10] D. Bouwmeester, J.-W. Pan, K. Mattle, M. Eibl, H. Weinfurter, and A. Zeilinger. Experimental quantum teleportation. *Nature*, **390**:575–579, 1997. [2](#), [35](#)
- [11] Charles H. Bennett and Stephen J. Wiesner. Communication via one- and two-particle operators on Einstein-Podolsky-Rosen states. *Physical Review Letters*, **69**:2881–2884, 1992. [2](#)
- [12] Klaus Mattle, Harald Weinfurter, Paul G. Kwiat, and Anton Zeilinger. Dense Coding in Experimental Quantum Communication. *Physical Review Letters*, **76**:4656–4659, 1996. [2](#)
- [13] D. C. Burnham and D. L. Weinberg. Observation of Simultaneity in Parametric Production of Optical Photon Pairs. *Physical Review Letters*, **25**:84–87, 1970. [2](#)
- [14] A. Aspect, P. Grangier, and G. Roger. Experimental Tests of Realistic Local Theories via Bell’s Theorem. *Physical Review Letters*, **47**:460–463, 1981. [2](#)
- [15] P. G. Kwiat, K. Mattle, H. Weinfurter, A. Zeilinger, A. V. Sergienko, and Y. Shih. New High-Intensity Source of Polarization-Entangled Photon Pair. *Physical Review Letters*, **75**:4337–4341, 1995. [2](#), [21](#), [22](#), [23](#), [34](#), [42](#)
- [16] P. G. Kwiat, E. Waks, A. G. White, I. Appelbaum, and P. H. Eberhard. Ultrabright source of polarization-entangled photons. *Physical Review A*, **60**:R773–R776, 1999. [2](#)
- [17] Z. Y. Ou, X. Y. Zou, L. J. Wang, and L. Mandel. Observation of nonlocal interference in separated photon channels. *Physical Review Letters*, **65**:321–324, 1990. [2](#), [27](#), [34](#)

- [18] J. Brendel, E. Mohler, and W. Martienssen. Time-resolved dual-beam two-photon interferences with high visibility. *Physical Review Letters*, **66**:1142–1145, 1991. [2](#)
- [19] Kwiat, P. G., Steinberg, A. M., and Chiao, R. Y. High-visibility interference in a Bell-inequality experiment for energy and time. *Physical Review A*, **47**:R2472–R2475, 1993. [2](#)
- [20] J. Brendel, N. Gisin, W. Tittel, and H. Zbinden. Pulsed Energy-Time Entangled Twin-Photon Source for Quantum Communication. *Physical Review Letters*, **82**:2594, 1999. [2](#), [29](#), [31](#)
- [21] I. Marcikic, H. de Riedmatten, W. Tittel, V. Scarani, H. Zbinden, and N. Gisin. Time-bin entangled qubits for quantum communication created by femtosecond pulses. *Physical Review A*, **66**:062308, 2002. [2](#), [29](#), [31](#)
- [22] Alois Mair, Alipasha Vaziri, Gregor Weihs, and Anton Zeilinger. Entanglement of the orbital angular momentum states of photons. *Nature*, **412**:313–316, 2001. [2](#)
- [23] Gabriel Molina-Terriza, Juan P. Torres, and Lluís Torner. Twisted photons. *Nature Physics*, **3**:305–310, 2007. [2](#)
- [24] H. Bechmann-Pasquinucci and W. Tittel. Quantum cryptography using larger alphabets. *Physical Review A*, **61**:062308, 2000. [2](#)
- [25] Nicolas J. Cerf, Mohamed Bourennane, Anders Karlsson, and Nicolas Gisin. Security of Quantum Key Distribution Using d-Level Systems. *Physical Review Letters*, **88**:127902, 2002. [2](#)
- [26] Thomas Durt, Dagomir Kaszlikowski, Jing-Ling Chen, and L. C. Kwek. Security of quantum key distributions with entangled qudits. *Physical Review A*, **69**:032313, 2004. [2](#)
- [27] Lana Sheridan and Valerio Scarani. Security proof for quantum key distribution using qudit systems. *Physical Review A*, **82**:030301(R), 2010. [2](#)

BIBLIOGRAPHY

- [28] Tamás Vértesi, Stefano Pironio, and Nicolas Brunner. Closing the Detection Loophole in Bell Experiments Using Qudits. *Physical Review Letters*, **104**:060401, 2010. [2](#), [74](#), [79](#)
- [29] N. Brunner, S. Pironio, A. Acín, N. Gisin, A. Méthot, and & V. Scarani. Testing the Dimension of Hilbert Spaces. *Physical Review Letters*, **100**:210503, 2008. [3](#)
- [30] D. Collins, N. Gisin, N. Linden, S. Massar, and S. Popescu. Bell Inequalities for Arbitrarily High-Dimensional Systems. *Physical Review Letters*, **88**:040404, 2002. [3](#), [9](#), [74](#)
- [31] E. Schrödinger. Mathematical Proceedings of the Cambridge Philosophical Society. In *Discussion of Probability Relations between Separated Systems*, **31**, pages 555–563, 1935. [6](#)
- [32] A. Einstein, B. Podolsky, and N. Rosen. Can quantum mechanical reality considered to be complete? *Physical Review*, **47**:777–780, 1935. [6](#)
- [33] J. S. Bell. On the Einstein Podolsky Rosen Paradox. *Physics*, **1**:195–200, 1964. [7](#)
- [34] J. S. Bell. *Speakable and Unsayable in Quantum Mechanics*. Cambridge University Press, 1987. [7](#)
- [35] J. F. Clauser, M. A. Horne, A. Shimony, and R. A. Holt. Proposed Experiment to Test Local Hidden-Variable Theories. *Physical Review Letters*, **23**:880–884, 1969. [7](#)
- [36] A. Aspect, P. Grangier, and G. Roger. Experimental Realization of Einstein-Podolsky-Rosen-Bohm *Gedankenexperiment*: A New Violation of Bell’s Inequalities. *Physical Review Letters*, **49**:91–94, 1982. [8](#)
- [37] Gregor Weihs, Thomas Jennewein, Christoph Simon, Harald Weinfurter, and Anton Zeilinger. Violation of Bell’s Inequality under Strict Einstein Locality Conditions. *Physical Review Letters*, **81**:5039–5043, 1998. [8](#)

- [38] M. A. Rowe, D. Kielpinski, V. Meyer, C. A. Sackett, W. M. Itano, C. Monroe, and D. J. Wineland. Experimental violation of a Bell's inequality with efficient detection. *Nature*, **409**:791–794, 2001. [8](#)
- [39] Dagomir Kaszlikowski, Piotr Gnaciński, Marek Żukowski, Wiesław Miklaszewski, and Anton Zeilinger. Violations of Local Realism by Two Entangled N-Dimensional Systems Are Stronger than for Two Qubits. *Physical Review Letters*, **85**:4418–4421, 2000. [8](#)
- [40] A. Acín, T. Durt, N. Gisin, and J. I. Latorre. Quantum nonlocality in two three-level systems. *Physical Review A*, **65**:052325, 2002. [11](#), [13](#)
- [41] Li-Bin Fu, Jing-Ling Chen, and Xian-Geng Zhao. Maximal violation of the Clauser-Horne-Shimony-Holt inequality for two qutrits. *Physical Review A*, **68**:022323, 2003. [11](#)
- [42] Li-Bin Fu, Jing-Ling Chen, and Shi-Gang Chen. Maximal violation of Clauser-Horne-Shimony-Holt inequality for four-level systems. *Physical Review A*, **69**:034305, 2004. [11](#)
- [43] Lluís Masanes. Tight Bell inequality for d -outcome measurements correlations. *Quantum Inf. Comput.*, **3**:345, 2002. [11](#)
- [44] D. Collins and N. Gisin. Quantum nonlocality in two three-level systems. *J. Phys. A*, **37**:1775, 2004. [11](#)
- [45] Yeong-Cherng Liang. *Correlations, Bell Inequality Violation & Quantum Entanglement*. PhD thesis, 2008. [12](#), [13](#)
- [46] John F. Clauser and Michael A. Horne. Experimental consequences of objective local theories. *Physical Review D*, **10**:526, 1974. [12](#)
- [47] M. Navascués, S. Pironio, and A. Acín. Experimental consequences of objective local theories. *Physical Review Letters*, **98**:010401, 2007. [13](#)
- [48] Adetunmise C. Dada and Erika Anderson. On Bell Inequality Violations With High-dimensional Systems. *International Journal of Quantum Information*, **9**:1807–1823, 2011. [14](#)

BIBLIOGRAPHY

- [49] Cai Yu, Jean-Daniel Bancal and Valerio Scarani. 11th Intl. Conference on Quantum Communication, Measurement and Computing. In *CGLMP₄ Inequality as a Dimension Witness*, pages P1–47, Vienna, 2012. [14](#)
- [50] Valerio Scarani, Nicolas Gisin, Nicolas Brunner, Lluís Masanes, Sergi Pino and Antonio Acín. Secrecy extraction from no-signaling correlations. *Physical Review A*, **74**:042339, 2006. [18](#)
- [51] D. N. Klyshko. *Photons and Nonlinear Optics*. Gordon and Breach Science Publishers, 1970. [19](#)
- [52] C. K. Hong and L. Mandel. Theory of parametric frequency down conversion of light. *Physical Review A*, **31**:2409–2418, 1985. [19](#)
- [53] R. W. Boyd. *Nonlinear Optics*. Academic Press, Boston, 1992. [20](#)
- [54] Pavel Trojek. *Efficient Generation of Photonic Entanglement and Multiparty Quantum Communication*. PhD thesis, 2007. [21](#)
- [55] C. Kursiefer, M. Oberparleiter, and H. Weinfurter. High-efficiency entangled photon pair collection in type-II parametric fluorescence. *Physical Review A*, **64**:023802, 2001. [21](#), [37](#)
- [56] C. Kursiefer, M. Oberparleiter, and H. Weinfurter. Generation of correlated photon pairs in type-II parametric down conversion-revisited. *Journal of Modern Optics*, **48**:1997–2007, 2001. [21](#), [37](#)
- [57] F. A. Bovino, P. Varisco, A. M. Colla, G. Castagnoli, G. D. Giuseppe, and A. V. Sergienko. Effective fiber-coupling of entangled photons for quantum communication. *Optics Communications*, **227**:343–348, 2003. [21](#), [37](#)
- [58] P. S. K. Lee, M. P. van Exter, and J. P. Woerdman. How focused pumping affects type-II spontaneous parametric down-conversion. *Physical Review A*, **72**:033803, 2005. [21](#), [37](#)
- [59] Thomas Jennewein, Christoph Simon, Gregor Weihs, Harald Weinfurter, and Anton Zeilinger. Quantum Cryptography with Entangled Photons. *Physical Review Letters*, **84**:4729–4732, 2000. [21](#)

- [60] D. S. Naik, C. G. Peterson, A. G. White¹, A. J. Berglund, and P. G. Kwiat. Entangled State Quantum Cryptography: Eavesdropping on the Ekert Protocol. *Physical Review Letters*, **84**:4733–4736, 2000. [21](#)
- [61] J. F. Hodelin, G. Khoury, and D. Bouwmeester. Optimal generation of pulsed entangled photon pairs. *Physical Review A*, **74**:013802, 2006. [23](#), [24](#)
- [62] Poh Hou Shun. *Towards a high quality polarization-entangled multiphoton source*. Master thesis, 2009. [24](#), [25](#)
- [63] D. F. V. James, P. G. Kwiat, W. J. Munro, and A. G. White. Measurement of qubits. *Physical Review A*, **64**:052312, 2001. [26](#)
- [64] J. Řeháček, B.-G. Englert, and D. Kaszlikowski. Minimal qubit tomography. *Physical Review A*, **70**:052321, 2004. [26](#)
- [65] A. Ling, K. P. Soh, A. Lamas-Linares, and C. Kurtsiefer. Experimental polarization state tomography using optimal polarimeters. *Physical Review A*, **74**:022309, 2006. [26](#)
- [66] M. D. de Burgh, N. K. Langford, A. C. Doherty, and A. Gilchrist. Choice of measurement sets in qubit tomography. *Physical Review A*, **78**:052122, 2008. [26](#)
- [67] J. D. Franson. Bell Inequality for Position and Time. *Physical Review Letters*, **62**:2205, 1989. [28](#), [29](#), [31](#)
- [68] W. Tittel, J. Brendel, B. Gisin, T. Herzog, H. Zbinden, and N. Gisin. Experimental demonstration of quantum correlations over more than 10 km. *Physical Review A*, **57**:3229–3232, 1998. [32](#)
- [69] Harald Weinfurter and Marek Żukowski. Four-photon entanglement from down-conversion. *Physical Review A*, **64**:010102(R), 2001. [32](#)
- [70] A. Lamas-Linares, J. C. Howell, and D. Bouwmeester. Stimulated emission of polarization-entangled photons. *Nature*, **412**:887–890, 2001. [32](#)

BIBLIOGRAPHY

- [71] Wei-Bo Gao, Chao-Yang Lu, Xing-Can Yao, Ping Xu, Otfried Gühne, Alexander Goebel, Yu-Ao Chen, Cheng-Zhi Peng, Zeng-Bing Chen, and Jian-Wei Pan. Experimental demonstration of a hyper-entangled ten-qubit Schrödinger cat state. *Nature Physics*, **6**:331–335, 2010. [32](#), [33](#), [63](#)
- [72] R.T. Thew, A. Acín, H. Zbinden, and N. Gisin. Experimental realization of entangled qutrits for quantum communication. *Quantum Information and Computation*, **4**:93, 2004. [32](#)
- [73] D. Richart, Y. Fischer, and H. Weinfurter. Experimental implementation of higher dimensional time-energy entanglement. *Applied Physics B*, **106**:543–550, 2012. [32](#)
- [74] D. Richart. *Entanglement of Higher Dimensional Quantum States*. Diploma thesis, 2008. [32](#)
- [75] Hugues de Riedmatten, Ivan Marcikic, Valerio Scarani, Wolfgang Tittel, Hugo Zbinden, and Nicolas Gisin. Tailoring photonic entanglement in high-dimensional Hilbert spaces. *Physical Review A*, **69**:050304(R), 2004. [33](#)
- [76] Alipasha Vaziri, Gregor Weihs, and Anton Zeilinger. Experimental Two-Photon, Three-Dimensional Entanglement for Quantum Communication. *Physical Review Letters*, **89**:240401, 2002. [33](#)
- [77] Adetunmise C. Dada, Jonathan Leach, Gerald S. Buller, Miles J. Padgett, and Erika Andersson. Experimental high-dimensional two-photon entanglement and violations of generalized Bell inequalities. *Nature Physics*, **7**:677–680, 2011. [33](#), [63](#)
- [78] Megan Agnew, Jonathan Leach, Melanie McLaren, F. Stef Roux, and Robert W. Boyd. Experimental high-dimensional two-photon entanglement and violations of generalized Bell inequalities. *Physical Review A*, **84**:062101, 2011. [33](#)
- [79] Robert Fickler, Radek Lapkiewicz, William N. Plick, Mario Krenn, Christoph Schaeff, Sven Ramelow, and Anton Zeilinger. Quantum

- Entanglement of High Angular Momenta. *Science*, **338**:640–643, 2012. [33](#)
- [80] D Giovannini, F M Miatto, J Romero, S M Barnett, J P Woerdman, and M J Padgett. Determining the dimensionality of bipartite orbital-angular-momentum entanglement using multi-sector phase masks. *New J. Phys.*, **14**:073046, 2012. [33](#)
- [81] Julio T. Barreiro, Nathan K. Langford, Nicholas A. Peters, and Paul G. Kwiat. Generation of Hyperentangled Photon Pairs. *Physical Review Letters*, **95**:260501, 2005. [33](#)
- [82] Stephen P. Walborn. Hyperentanglement: Breaking the communication barrier. *Nature Physics*, **4**:268–269, 2008. [33](#)
- [83] Julio T. Barreiro, Tzu-Chieh Wei, and Paul G. Kwiat. Beating the channel capacity limit for linear photonic superdense coding. *Nature Physics*, **4**:282–286, 2008. [33](#)
- [84] Paul G. Kwiat and Harald Weinfurter. Embedded Bell-state analysis. *Physical Review A*, **58**:R2623–R2626, 1998. [33](#)
- [85] Carsten Schuck, Gerhard Huber, Christian Kurtsiefer, and Harald Weinfurter. Complete Deterministic Linear Optics Bell State Analysis. *Physical Review Letters*, **96**:190501, 2006. [33](#)
- [86] Tzu-Chieh Wei, Julio T. Barreiro, and Paul G. Kwiat. Hyperentangled Bell-state analysis. *Physical Review A*, **75**:060305(R), 2007. [33](#)
- [87] M. Barbieri, G. Vallone, P. Mataloni, and F. De Martini. Complete and deterministic discrimination of polarization Bell states assisted by momentum entanglement. *Physical Review A*, **75**:042317, 2007. [33](#)
- [88] Benjamin P. Lanyon, Marco Barbieri, Marcelo P. Almeida, Thomas Jennewein, Timothy C. Ralph, Kevin J. Resch, Geoff J. Pryde, Jeremy L. O’Brien, Alexei Gilchrist, and Andrew G. White. Simplifying quantum logic using higher-dimensional Hilbert spaces. *Nature Physics*, **5**:134–140, 2009. [33](#)

BIBLIOGRAPHY

- [89] Charles H. Bennett, David P. DiVincenzo, Peter W. Shor, John A. Smolin, Barbara M. Terhal, and William K. Wootters. Remote State Preparation. *Physical Review Letters*, **87**:077902, 2001. [33](#)
- [90] Marco Barbieri, Francesco De Martini, Paolo Mataloni, Giuseppe Vallone, and Adán Cabello. Enhancing the Violation of the Einstein-Podolsky-Rosen Local Realism by Quantum Hyperentanglement. *Physical Review Letters*, **97**:140407, 2006. [33](#)
- [91] A. K. Ekert. Quantum Cryptography Based on Bell's Theorem. *Physical Review Letters*, **67**:661–663, 1991. [35](#)
- [92] Dirk Bouwmeester, Artur K. Ekert, Anton Zeilinger. *The Physics of Quantum Information: Quantum Cryptography, Quantum Teleportation, Quantum Computation*. Springer-Verlag, 2000. [36](#)
- [93] N. Boeuf, D. Branning, I. Chaperot, E. Dauler, S. Guérin, G. Jaeger, A. Muller, A. Migdall. Calculating characteristics of noncollinear phase matching in uniaxial and biaxial crystals. *Opt. Eng.*, **39**:1016–1024, 2000. [37](#)
- [94] C. H. Monken, P. H. Souto Ribeiro, and S. Pádua. Optimizing the photon pair collection efficiency: A step toward a loophole-free Bells inequalities experiment. *Physical Review A*, **57**:R2267–R2269, 1998. [38](#)
- [95] P. S. K. Lee, M. P. van Exter, and J. P. Woerdman. Increased polarization-entangled photon flux via thinner crystals. *Physical Review A*, **70**:043818, 2004. [38](#)
- [96] Bahaa E. A. Saleh and Malvin Carl Teich. *Fundamentals of Photonics*. Wiley, 2007. [40](#)
- [97] P. Trojek and H. Weinfurter. Collinear source of polarization-entangled photon pairs at nondegenerate wavelengths. *Appl. Phys. Lett.*, **92**:211103, 2008. [42](#)
- [98] Sascha Gaertner, Harald Weinfurter, and Christian Kurtsiefer. Fast and compact multichannel photon coincidence unit for quantum information processing. *Rev. Sci. Instrum.*, **76**:123108, 2005. [56](#)

- [99] J. Liang, S.M. Hendrickson, and T.B. Pittman. Role of pump coherence in two-photon interferometry. *Physical Review A*, **83**:033812, 2011. [58](#)
- [100] Martin Hendrych, Rodrigo Gallego, Michal Mičuda, Nicolas Brunner, Antonio Acín, and Juan P. Torres. Experimental estimation of the dimension of classical and quantum systems. *Nature Physics*, **8**:588–591, 2012. [63](#)
- [101] Johan Ahrens, Piotr Badziacedilg, Adán Cabello, and Mohamed Bourennane. Experimental device-independent tests of classical and quantum dimensions. *Nature Physics*, **8**:592–595, 2012. [63](#)
- [102] Yu Cai. PhD thesis, National University of Singapore, to be published. [64](#)
- [103] T. Durt, D. Kaszlikowski, and M. Żukowski. Violations of local realism with quantum systems described by N-dimensional Hilbert spaces up to N=16. *Physical Review A*, **64**:024101, 2001. [74](#)
- [104] J. Minase, T.-F. Lu, B. Cazzolato, S. Grainger. A review, supported by experimental results, of voltage, charge and capacitor insertion method for driving piezoelectric actuators. *Precision Engineering*, **34**:692–700, 2010. [77](#)
- [105] S. Tanzilli, W. Tittel, H. De Riedmatten, H. Zbinden, P. Baldi, M. De Micheli, D.B. Ostrowsky, and N. Gisin. PPLN waveguide for quantum communication. *Eur. Phys. J. D*, **69**:155–160, 2002. [79](#)
- [106] Christopher E. Kuklewicz, Marco Fiorentino, Gatan Messin, Franco N. C. Wong, and Jeffrey H. Shapiro. High-flux source of polarization-entangled photons from a periodically poled KTiOPO4 parametric down-converter. *Physical Review A*, **69**:013807, 2004. [79](#)
- [107] W. H. Peeters and M. P. van Exter. Optical characterization of periodically-poled KTiOPO4. *Opt Express*, **16**:7344–7360, 2008. [79](#)
- [108] J. Romero, D. Giovannini, S. Franke-Anold, S. M. Barnett, M. J. Padgett. Increasing the dimension in high-dimensional two-photon

BIBLIOGRAPHY

orbital angular momentum entanglement. *arXiv:1205.1968v1*, 2012.

80